Aeroelasticity of a Generic Wing in Ground Effect

Andre Fellipe Vilanova de Araujo Aquino

Faculty of Science and Engineering

Master of Research

Supervised by

Dr. Sammy Diasinos

Submitted: November 15, 2018

Statement of Originality

I, Andre Fellipe Vilanova de Araujo Aquino, hereby declare that this thesis submission is my own work and has not previously been submitted for a degree or diploma in any university. To the best of my knowledge and belief, the thesis contains no material previously published or written by another person except where due reference is made in the thesis itself.

Signed: _____

Date: _____

Acknowledgements

Firstly, I would like to express my gratitude towards the efforts of my supervisor, Dr Sammy Diasinos. Without his help I could not create such good looking plots. Joking aside, your guidance academically and professionally was essential to develop this research, matching what I expected from this partnership when I decided to come to Australia. His knowledge of CFD and aerodynamics as well as his career path has inspired me.

I also would like to acknowledge my colleagues Sajjad Saleh, James Slaughter, Liang and Tim. All of them were of great technical support as well as kept me motivated during the progress of this work. However, I have to highlight the assistance of Sajjad and James. Thank you, Sajjad, for your kindness – hope you understand the irony – for the quick support and comedy relief. James, I am thankful for your ceaseless support even when you had finished your master's degree. Thank you both for inspiring me and for the afternoon coffees. I expect to have future nonsense talks.

Finally, I would like to thank my family and friends. My family - dad, mom, and my little sister - for supporting me in all ways with my decision to cross the whole world to achieve my dreams and for keeping supporting me every day. All my friends for helping me to keep my spirits high and for having conversations about our struggles and accomplishments, they were essential. A special acknowledgement to Davidson, our friendship did not change with the distance and the 12 hours difference between Brazil and Australia. Additionally, you motivated me even when I thought I would not succeed.

Thank you all. It has been a difficult road, but all of you helped me to get where I am now.

Abstract

The front wing of a Formula car has a significant impact on the overall aerodynamic performance of the vehicle. Previous research proved that the wing proximity to the ground plays a crucial role in the generation of loads and flow structures. However, all previous published research disregarded the effects of wing deformation. This study investigates the aeroelastic behaviour of a downforce producing wing in ground effect by developing and comparing the static loosely-coupled and the tightly-coupled FSI methods. The static loosely-coupled method was incapable of reproducing the loads and deflection oscillations captured by the tightly-coupled FSI, but computed the time-averaged deflection and loadings with discrepancies less than 3% despite using 21 times less computational resources. Further static loosely-coupled FSI simulations were undertaken to analyse the lift loss phenomenon of a flexible wing at two Reynolds numbers. For the Reynolds number of 4.46×10^5, based on a chord length of 0.223m, the critical height shifted from $h = 0.080c$ to $h = 0.091c$, whereas it shifted from $h = 0.080c$ to $h = 0.101c$ for the Reynolds number of 6.69×10^5. This variation in critical height has been linked to an earlier main wing vortex break down caused by the reduced tip ground clearance due to the deflection.

Keywords:
Aeroelasticity, Wing in ground effect, lift loss phenomenon, downforce, vortex breakdown.

List of Publications

Journal papers in development:

Aquino, A., Diasinos, S., Saleh, S. Comparing a tightly-coupled and a static loosely-coupled strategy to investigate flexible wings in ground effect. To be submitted to Proceedings of the Institution of Mechanical Engineers, Part G: Journal of Aerospace Engineering

Aquino, A., Diasinos, S., Saleh, S., The implications of aeroelasticity on wings in ground effect" To be submitted to Proceedings of the Institution of Mechanical Engineers, Part G: Journal of Aerospace Engineering

Abbreviations

ABS	Acrylonitrile Butadiene Styrene
AIAA	American Institute of Aeronautics and Astronautics
AoA	Angle of Attack
AWS	Amazon Web Service
CFD	Computational Fluid Dynamics
CoP	Centre of Pressure
CPU	Central Processing Unit
CRM	Common Research Model
DES	Detached Eddy Simulation
DNS	Direct Numerical Simulation
FEA	Finite Element Analyses
FEM	Finite Element Method
FFT	Fast Fourier Transform
FSI	Fluid Structure Interaction
FVM	Finite Volume Method
F1	Formula 1
GCI	Grid Convergence Index
GP	Grand Prix
LES	Large Eddy Simulation
MAV	Micro Air Vehicles
PIV	Particle Image Velocimetry
SIMPLE	Semi-Implicit Method for Pressure-Linked Equations
SIMPLEC	SIMPLE-Consistent
RANS	Reynolds-Averaged Navier-Stokes
Re	Reynolds number
RMS	Root Mean Square
S-A	Spallart Allmaras
SST	Shear Stress Transport
T026	Tyrrel 026
URANS	Unsteady Reynolds-Averaged Navier-Stokes
2D	2 Dimensional
3D	3 Dimensional

Nomenclature

a	heaving amplitude
b_i	body forces
c	wing chord
C_D	drag coefficient
C_L	lift coefficient
Cp	pressure coefficients
E_{ij}	strain
E_s	Young's modulus of the material
f	frequency
f_i	external load applied to solid
f_n	normalised frequency
F_s	safety factor in GCI formulation
F_j^s	load vector
g	parameter analysed in GCI formulation
h	ground clearance
H_n	number of cells in a given mesh
I	second moment of inertia
k	turbulent kinetic energy
K_{ij}^S	stiffness matrix
l	half wingspan
M_i	moment around a given axis
M_{ij}^s	mass matrix
p	flow pressure
$\bar{p}$	mean flow pressure
p'	fluctuating flow pressure
P	order of convergence in GCI formulation
r	ratio of coarse to fine meshes in GCI formulation
Re_θ	transition onset momentum thickness Reynolds number
S_{ji}	second Piola-Kirschhoff stress tensor
S_{ij}^*	mean strain rate tensor
t	time

u_i	velocity components in each spatial coordinate
$\bar{u}_i$	steady mean velocity in each spatial coordinate
$u_i{}'$	fluctuating velocity term in each spatial coordinate
U_∞	free-stream velocity
x_i	spatial coordinates
X_j	spatial coordinates for the solid system
y_p	first cell height on a wall
y^+	wall y plus

Greek Symbols

β, γ_p	Newmark integration parameters
γ	intermittency
δ_{ij}	Kronecker delta
Δt	time step
ε	turbulent dissipation rate
ζ	boundary layer thickness
ϑ	solid deformation
$\dot{\vartheta}$	solid velocity
$\ddot{\vartheta}$	solid acceleration
λ_s, μ_S	Lame's constants
μ	dynamic viscosity of the fluid
μ_t	turbulent viscosity
ν_s	Poisson's ratio of the material
ρ	density of fluid
ρ_s	solid density
σ_{ij}	Cauchy stress tensor
τ_{ij}	Reynolds stresses
ω	specific dissipation rate

Table of Contents

List of Figures

List of Tables

1. Introduction

1.1 Introduction and Background

Race car categories are a powerful media of advertisement for automotive manufacturers, technology specialists and to numerous other companies. Being associated with the virtues of motorsport, e.g., cutting edge technology, speed and high competitiveness aggregates value to the company name. For automotive manufacturers and technology specialist, the benefits exceed the marketing exposure since the technical knowledge transfer between race teams and companies is a fundamental aspect of this partnership.

Among all categories, Formula 1 (F1) is the most prestigious and competitive. The teams usually have a budget over $400 million (Sylt, 2018) per year to continuously improve the vehicle performance. In F1, tenths of seconds usually separate the pole position and the second position in the qualifying session of a Grand Prix (GP). For instance, in the 2018 Austrian GP, the pole position was defined on a time lap difference that did not exceed 0.02s (BBC, 2018). In order to optimise the vehicle performance and minimise the time lap, the aerodynamic design has a crucial role, being one of the most decisive areas. At the present moment, there are several aerodynamic devices such as wings, diffusers, splitters and barge boards (Figure 1.1). The first race car to use an inverted wing was a Chaparral Can-Am car in 1966 and, two years later, this idea was adopted in F1 (Zerihan, 2001). Since then, it has been widespread to other racing categories.

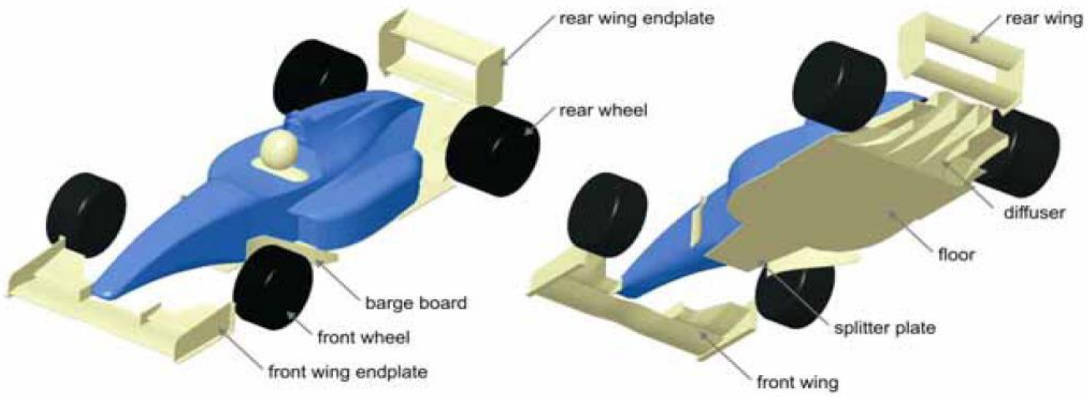

Figure 1.1 Aerodynamic package of an open-wheel vehicle (Diasinos, 2009)

The amount of downforce generated represents an essential aspect of designing a race car aerodynamic package, along with other metrics such as stability, aero balance and cooling.

Downforce is produced in order to increase the normal load on each tyre. This results in higher longitudinal and transverse forces, enhancing the vehicle's acceleration, braking and cornering ability (Katz, 1995). Agathangelou and Gascoyne (1998) estimated that, depending on the circuit, and if all other vehicle parameters are preserved, a 10% increase in downforce will reduce lap times by between 0.7s and 1s.

The front wings of open-wheel race cars are responsible for producing 30% of the total downforce (Agathangelou and Gascoyne, 1998; Dominy, 1992) and for heavily influencing the aerodynamic performance of all other components (Zhang et al., 2002). The effectiveness of barge boards, floor and diffuser is highly dependent on the vortices produced by the endplate and the multiple elements of an F1 front wing. Previous research proved that the wing proximity to the ground has a significant impact on the loads and the flow structures generated by this device. However, all previous studies have assumed that the wing is rigid, whereas in reality a front wing is flexible.

The interaction between a flexible body and the fluid domain is a bi-directionally coupled process. The body is deformed by the force produced by the fluid flow, and the modified body influences the fluid field, generating a dissimilar load (Uekermann, 2016). This phenomenon occurs in multiple cycles, potentially results in structural failures and/or lower efficiency of the system. When the Fluid-Structure interaction (FSI) is a combination of Solid Mechanics, Structural Dynamics and Aerodynamics, it is known as aeroelasticity (Collar, 1946), which can either happen statically or dynamically. If the aeroelastic system behaves as time independent, it is described as static. On the other hand, the phenomenon is defined as dynamic when it varies with time.

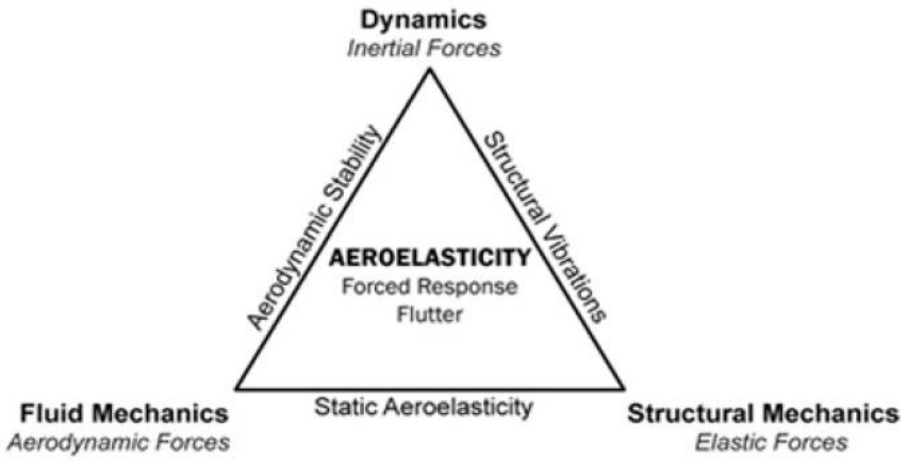

Figure 1.2: Collar diagram showing the interaction between aeroelastic disciplines (Collar, 1946)

A series of airplane disasters caused by aeroelasticity stimulated the investigation of this field. According to Garrick and Reed III (1981), aeroelastic phenomena provoked the accidents involving Langley's aircraft and the Hanley Page O/400 bomber. Birnbaum (1924) and Collar (1946) were one of the first researchers responsible for detecting the causes of these phenomena and improving the general understanding in the field (Weisshaar, 1995). However, due to the multidisciplinary aspect of aeroelasticity, the progress was profoundly limited. With recent developments in computational hardware and numerical methods, relevant methodologies have been refined, but are still limited in efficacy and resolution.

1.2 Aims and Objectives

The inexistence of previous published studies about aeroelasticity of wings in ground effect raises the following questions: What is the most suitable methodology to investigate the time-averaged implications of aeroelasticity on wings in ground effect? What are the main effects of structural flexibility on the aerodynamic performance of downforce producing wings in this scenario? What are the reasons for these effects? In order to answer these questions, a series of investigative steps are undertaken:

- Perform a tightly-coupled FSI strategy using the system coupling built in ANSYS 17.2.
- Create and implement a static loosely-coupled FSI methodology that couples ANSYS Fluent 17.2 and ANSYS Mechanical solver 17.2.
- Compare both methods and justify the selection to investigate the time-averaged implications of aeroelasticity on a wing in ground effect.
- Make recommendations for future work in order to improve the method performance and to further understand the aeroelasticity of wings in ground effect.

2. Literature Review

2.1 Downforce Producing Wing in Ground Effect

Dominy (1992) was the first author to publish an explanation about the effect of ground proximity in a downforce producing wing. He stated that the downforce increase of a wing near a ground plane was due to the constraining effect the flow experiences between the wing surface and the ground. The area reduction underneath the wing accelerated the flow and, consequently, generated a greater suction peak. The experiments conducted by Knowles et al. (1994) on a GA(W)-1 wing in ground clearances between $h = 1.0c$ and $h = 0.12c$ confirmed that the venturi effect was indeed the reason for an increase in downforce when the wing clearance decreased.

Razenbach and Barlow (1994) conducted experimental and numerical analyses on a symmetrical NACA 0015 aerofoil at an angle of attack of 0°. The authors observed that this profile generated downforce at heights lower than $0.9c$, contradicting the zero lift value reported by Abbot and Von Doenhoff (1958) when the wing was operating in free stream. Ranzenbach and Barlow indicated the venturi effect as the cause for the downforce measurement. Moreover, a drop in downforce for wing heights lower than $0.0324c$ was reported. This behaviour was named "force reversal phenomenon", and the authors proposed that the flow deceleration, caused by the merging of the wing and ground boundary layers, was the reason for this phenomenon.

Razenbach and Barlow (1997, 1996, 1995) investigated different techniques to represent the ground plane. Tests were performed with an aerofoil in proximity to moving and stationary grounds. The results showed that the critical height – the height in which the drop in downforce happens – and the force values captured by both techniques were different. The downforce was 10% less when a static ground was employed, which was a consequence of the thicker ground boundary layer that decelerated the air underneath the wing. This discrepancy highlights the importance of using a moving ground since it better represents the track physical conditions. In these scenarios, there is no relative velocity between the ground and the free stream flow and, as a consequence, the ground boundary layer only grows when the air is accelerated due to the venturi effect.

The studies of Ranzenbach and Barlow (1997, 1996, 1995) also proved that the “force reversal phenomena” is geometrically dependent. Experimental and numerical analyses were conducted on a NACA 4412 and a NACA 63_2-215 Mod B with a 30% chord flap. For the NACA 63_2-215, the critical

height was $0.25c$, whilst a lower critical height of $0.097c$ was captured for the NACA 4412 profile. Furthermore, flow analyses of the NACA 63_2-215 portrayed that the ground and wing boundary layers were not merging at the critical height. This contradicted the reason stated by the authors to explain the force reversal phenomenon. Nevertheless, the authors ignored this fact and persisted on relating this phenomenon to the boundary layer merging.

Zerihan and Zhang (2000) provided a more rigorous explanation for the force reversal phenomenon than that presented by Razenbach and Barlow. The experimental tests conducted at a Reynolds number of 4.62×10^5 in a T026 wing with endplates indicated that the lift loss phenomenon was a result of the excessive flow separation on the suction surface of the wing. According to Zerihan and Zhang, the separation caused by the adverse pressure gradient decelerated the flow underneath the wing and reduced the maximum suction peak. This hypothesis is coherent with the wing stall in free stream after increments in the angle of attack and justifies why the drag kept increasing even at heights less than the critical height. In the end, the authors decided to rename the "force reversal phenomenon" as "lift loss phenomenon" since no force reversal was actually occurring.

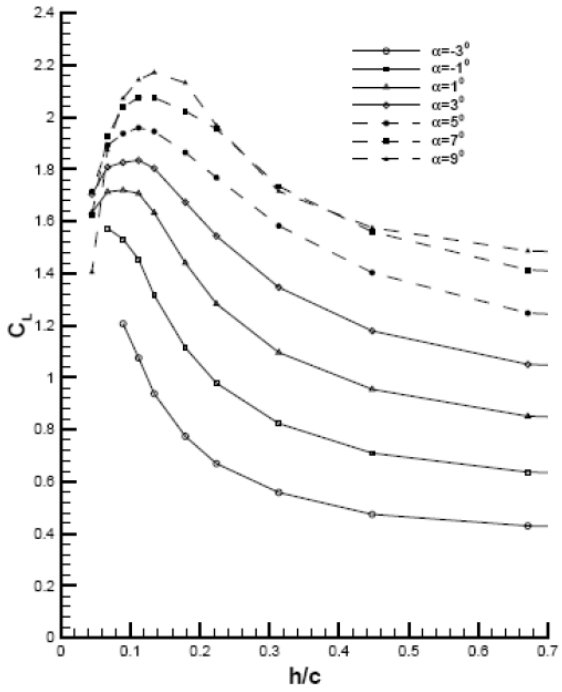

Figure 2.1: Lift loss Phenomenon plot obtained by Zerihan and Zhang (2000)

The results achieved by Zerihan and Zhang (2000) demonstrated that higher angles of attack led to a rise in the critical height. The gain in incidence angle intensified the boundary layer separation and hence increased the height in which the lift loss happened. Through the use of flow visualisation paint (Figure 2.2), separation across the bottom surface of the wing was observed to be inconsistent as the

flow did not separate in the region close to the endplate. The authors suggested that the tip vortex reduced the incidence flow angle, in an effect described as upwash, and prevented the boundary layer separation.

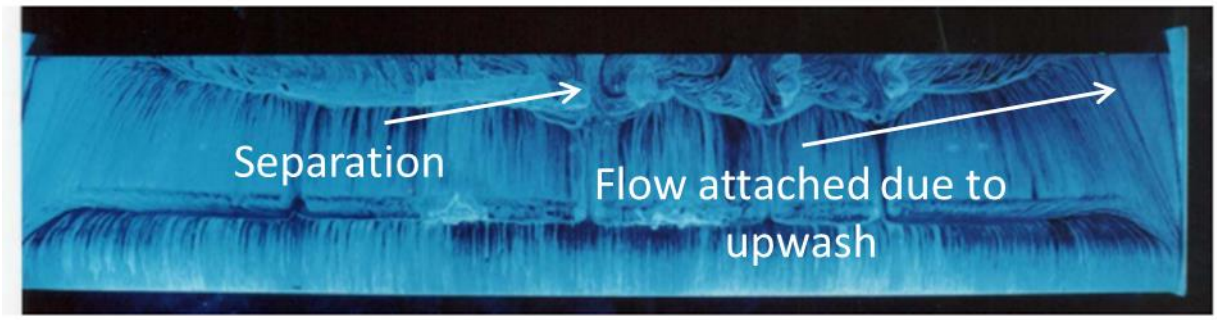

Figure 2.2: Flow visualisation by Zerihan and Zhang (2000)

All tests conducted by Zerihan and Zhang (2000) had an endplate fixed at the tip of the wing because of the increase in normal force that these devices produce. Mcbeath (1998) explained that endplates work as a physical barrier between the suction and the pressure regions around the wing. This limits the merging between the high and low velocity flows. Mcbeath (1998) reported that the use of endplates can increase the downforce by up to 30%.

Zhang et al. (2002), who also used the T026 profile, employed Laser Doppler Anemometry (LDA) and Particle Image Velocimetry (PIV) techniques to investigate the wing-tip vortices. The authors indicated that the rate of change in downforce is conditioned to variations in the tip vortex structure. At heights above $0.179c$, the vortex strengthened at a specific rate, and the downforce followed a similar trend. At heights below $0.179c$ and above the critical height ($0.134c$), the vortex significantly increased in size, started to break down and led to an increase in downforce with a reduced rate. At the critical height, the vortex completely burst and further reductions in ground clearance resulted in a downforce loss. Moreover, Zhang et al. (2002) revealed that the sectional vertical load at the tip matched the same trend observed for the overall downforce coefficient. On the other hand, the maximum downforce coefficient at the centre section was verified at larger heights than the critical height since the boundary layer separation in this region occurred earlier. The flow at the tip of the wing only separated when the vortex broke down and the upwash effect disappeared.

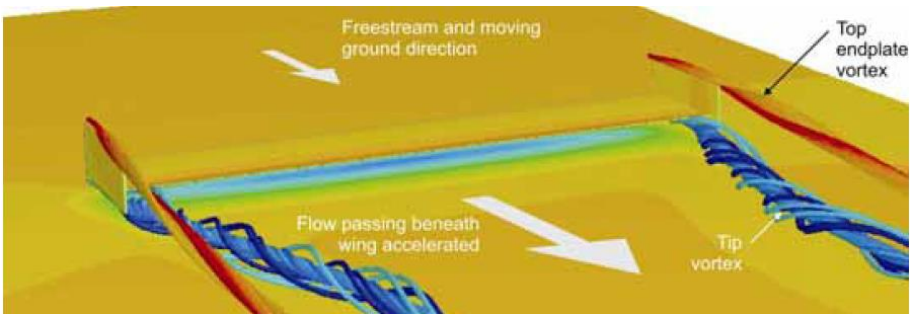

Figure 2.3: Vortex structure described by Zhang et al. (2002)

Similarly, Diasinos et al. (2013) demonstrated the relationship between the main tip vortex and the lift loss phenomena. They recognised during this study that the critical height decreased as the wingspan was reduced. The reason for this trend was related to the main tip vortex. At shorter wingspans, the vortex strength did not change significantly, re-energising the boundary layer and keeping the flow attached over a greater proportion of the wing (Figure 2.4). The delayed flow separation allowed the wing to operate at lower heights. The reduction in wingspan from $2.46c$ to $0.67c$ moved the critical height from $0.085c$ to $0.062c$.

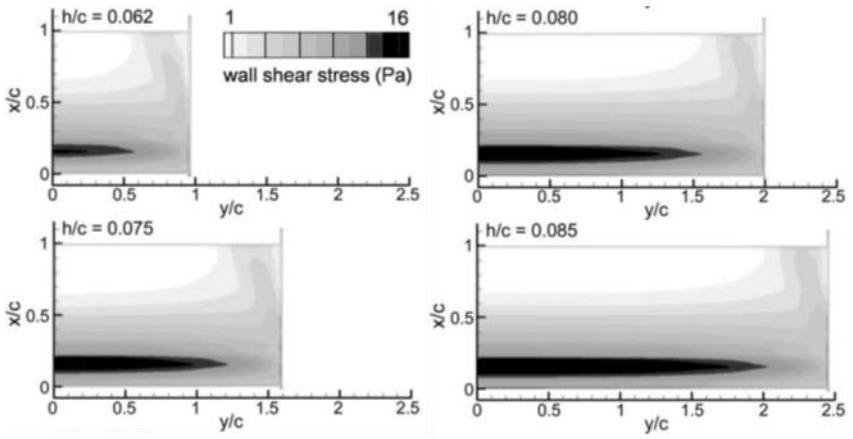

Figure 2.4: Wall Shear Stress on wings with different wingspans by Diasinos et al. (2013)

All these studies relevant to wings in ground effect suggest that deformed and rigid wings should be expected to have different lift loss behaviours. Due to deflection, the wing tip is closer to the ground than the centre section and, consequently, it is expected an earlier separation and earlier breakdown of the main tip vortex. Furthermore, the aerodynamic loads can twist the wing, changing the incidence angle. As commented by Zerihan and Zhang (2000), the critical height is highly dependent on these characteristics.

2.1.1 Unsteady analyses of wings in ground effect

In general, steady-state Reynolds-Averaged Navier Stokes (RANS) simulations are effective in predicting the lift loss phenomenon of a single element wing. Diasinos et al. (2014) and Keogh et al. (2015) developed computational models based on the RANS method that accurately captured the critical height and the lift coefficient. The maximum error in downforce was 3 % in comparison to the experiments. However, some scenarios require the use of transient simulations to better understand the unsteady flow around a wing in ground effect. Complex geometry wings and oscillatory profiles may create this type of unsteadiness.

Bruckner and Zhang (2010) employed the Detached Eddy Simulation (DES) method in order to investigate the complex flow around a double-element wing in ground effect. The results obtained with the DES method were compared to RANS simulations and validated against the experimental data produced by Mahon and Zhang (2006), who used the same wing geometry. At heights above $h/c = 0.211$, both RANS and DES methods reproduced the downforce trend and under-predicted the force values by no more than 7%. At further reduced heights, the DES analyses accurately reproduced the downforce behaviour with a constant error of 3%, whereas the RANS simulations could not follow the same downforce trend exhibited by the experiments. The authors explained this discrepancy by demonstrating how the RANS method was not able to predict the vortex breakdown. In general, DES is more accurate to model the wing vortices but comparatively, have much higher computational cost. The authors reported that this method on average took 300 hours to solve 12000 time steps in a machine with 24 processors located on the Iridis2 cluster at the University of Southampton.

Molina and Zhang (2011) analysed a wing with vertical oscillatory motion in ground effect. This oscillation motion, also named as heaving, was achieved by varying the ground clearance in a sinusoidal formulation with amplitude a and frequency f. A transient computational model using the Spalart-Allmaras turbulence model was developed to study a double element wing with the same profile used by Mahon (2006). Different heaving frequencies were simulated, and the results revealed that the aerodynamic response to the wing oscillation was divided into three different regimes - ground effect, incidence effect and added mass effect – depending on the normalized frequency (f_n) (Equation 1). At low frequencies ($f_n < 0.55$), there was no significant difference between the static and the heaving wing, i.e., the aerodynamic loads were mainly affected by the ground distance and the lift loss curve was barely influenced by the aerofoil oscillation. Therefore, a quasi-static motion could be employed to analyse the flow of the oscillating wing. At medium frequencies ($0.55 < f_n <$

1.09), the aerodynamic behaviour was dependent on the ground proximity and on the wing frequency. The aerofoil vertical motion led to a change in the effective incidence angle and hence in the aerodynamic loads. At higher frequencies ($f_n > 1.09$), an added mass effect was witnessed and it was prevailing over the ground effect. The authors demonstrated that the downforce enhanced as the frequency increased, and this behaviour was larger in ground proximity than in freestream.

$$f_n = \frac{\pi f c}{U_\infty} \tag{1}$$

Molina et al. (2011) expanded the understanding of aerodynamic performance of heaving aerofoils in ground effect. The results showcased that the force reduction due to ground proximity is only noticeable at low frequencies. At medium and high frequencies the aerodynamic loads are mainly dependant on the heaving frequency since the viscous effects become negligible. It was also observed that, at low ride heights and low frequencies, the aerofoil motion was unstable, and stall flutter was likely to occur due to the repeated separation and reattachment of the boundary layer. It is important to distinguish stall flutter from classical flutter. The classical flutter, which happens with flow attached at all times, is a result of the lag between aerodynamic forces and wing motion in various degrees of freedom in such manner that the wing absorbs energy from the flow. On the other hand, stall flutter, as the name implies, is caused by the periodical complete or partial separation of the flow (Dowell et al., 1989).

Whilst in the paper of Molina et al. (2011) stall flutter is a result of the artificial heaving oscillation, in reality, it can be caused by the aeroelastic behaviour of the wing. In an airplane wing, the pitching oscillation due to aeroelastic twist can lead to the continuous reattachment and separation, whereas in wings in ground effect, the deflection oscillation can be the reason for it.

2.2 The Investigation of FSI

2.2.1 Methods to Investigate FSI and Aeroelasticity

The primordial studies about aeroelasticity were analytically and experimentally based (Birnbaum, 1924; Theodorsen, 1949; Von Baumhauer and Koning, 1923). Nevertheless, with advances in computational hardware and modelling techniques, numerical methods became a powerful tool to better investigate aeroelasticity and FSI in general.

According to Uekerman (2016), there are two main numerical strategies in order to solve FSI problems. Firstly, the partitioned strategy that solves each field in separate codes (modules) and

transfers data between them. Secondly, the monolithic strategy that blends the two phenomena in a singular code. Both strategies for implementing a multi-physics computational model have advantages and disadvantages. The partitioned method is more flexible and performs better in weak coupling problems, but it can face convergence issues such as the added mass instability (Uekermann, 2016) . On the other hand, the monolithic strategy is usually suitable for strongly coupled phenomena - FSI systems that cannot be treated separately - due to its robustness. The necessity to implement a completely new code that fits the physical equations and solve them all together is the main reason to deter developers from implementing the monolithic approach. Uekerman states that only the partitioned approach allows a feasible time-to-solution, such that the overall time from developing the monolithic algorithm to the final simulation is not suitable for most applications.

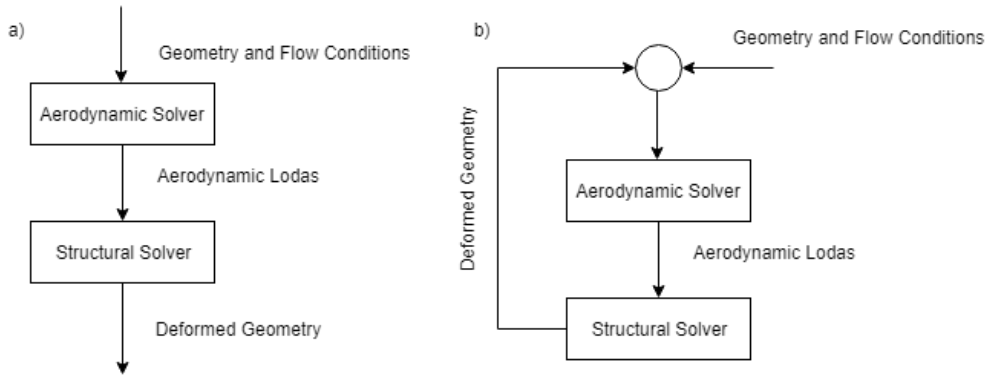

Figure 2.5: Flowchart exhibiting one-way and two-way FSI strategies

Cross et al. (2007) states that the partitioned approach can be classified in either one-way or two-way (Figure 2.5). If the coupling is one-way, data is transferred one time in the whole simulation, and the output from the Computational Fluid Dynamic (CFD) solver becomes the input to the structural solver. The two-way coupling consists of a loop of several one-way simulations. Data from the fluid dynamics code is transferred to the structural one, then data is transferred back, and the process continues for a specified number of time steps. The one-way simulations do not always accurately represent the FSI phenomenon since the process is interdependent, but it requires less computational effort. Therefore, it has been investigated how the results obtained through a one-way and two-way FSI differ.

Lin (2017), for example, compared the results achieved with a one-way and a two-way model to investigate the FSI between the blood flow and the artery wall, which was assumed as homogeneous to simplify the problem. The author concluded that, due to the assumption of a rigid wall, the one-way model did not effectively predict the vortices sizes and overestimated the shear stresses. Both

methodologies computed similar deformation, but Lin (2017) suggested that the use of an anisotropic material or the reduction in the wall modulus of elasticity may alter this trend.

Kesti and Olsson (2014) also detected discrepancies in the outcomes achieved by a one-way and a two-way FSI model to analyse the underbody panels used in passenger cars. This study showcased that the stress distribution obtained by a one-way and fully-coupled two-way FSI analysis were similar, but the displacements calculated did not match. While the one-way simulation determined the maximum displacement at the leading edge of the panel, the two-way FSI computed the maximum displacement at the centre of the panel. Due to this discrepancy in shape, a difference of 10% in lift coefficient was found for both methods.

These studies indicate that it is indeed necessary to compute the geometry deformation into the fluid analyses, making the one-way simulations unfeasible for most applications. Within the scope of a two-way FSI, different strategies can be employed, i.e., it can be performed through loosely or tightly coupled algorithms. It is called loosely coupled when the equations progress in time with information exchanged only after the end of the time step. In contrast, tightly coupled simulations perform sub-iterations at each time step until the convergence criteria are reached. Whereas the loosely coupled strategy is less computationally demanding, the strongly coupled is more robust as it better deals with non-linarites, such as flutter (Keyes et al., 2013). With respect to the computational cost, Landajuela et al. (2017) proved that, for an oscillating plate, the tightly-coupled FSI can be at least 2 times more expensive.

A number of studies have already employed the loosely-coupled method to investigate aeroelasticity in a wide variety of geometries, such as a wide-body airliner (Heinrich et al., 2001), wings (Wang and Lin, 2008), and rotors (Jung et al., 2013; Potsdam et al., 2006). The work of Love et al. (2000) is described in order to present the capabilities of the loosely-coupled method. These authors developed a computational method to analyse the aeroelastic behaviour of a fighter-aircraft in transonic regime (Mach 0.9), at incidence angle of 9° and a simulated 9g pulled-up condition. The Cp distributions from the midspan to the wing root presented excellent correlation to the experiments, but close to the tip major discrepancies rose. In this location, the numerical results overpredicted the shock strength due to the lack of viscosity effects in the Euler equations. The computational model was able to accurately simulate the wing deflection. The error at the tip did not exceed 0.7%. In contrast, the twist measurements were slightly underpredicted, but no percentage error is indicated by the authors. It is expected a better twist correlation when the CFD is based on the Navier-Stokes equations rather than Euler fluid formulation.

The use of the tightly-coupled methodology has already be proven to be feasible by Habchi et al. (2013) and Keye and Rudnik (2015). It is highlighted the study of Keye and Rudnik (2015) that employed this method to determine the static aeroelastic deformation of NASA's Common Research Model (CRM) in transonic regime. The numerical model was validated against the experimental data obtained at the European Transonic Wind Tunnel for Reynolds numbers equal to 5×10^6, 19.8×10^6 and 30×10^6. The lift and drag measurements computed numerically presented good quantitative agreement for all Reynolds numbers tested. It was even possible to detect the reduction in lift slope for angles higher than 3°. For the bending and twist results, the numerical model also exhibited a good correlation with experiments for all Reynolds numbers, except for $Re = 5 \times 10^6$ (Figure 2.7), where the measurements were underpredicted for AoA > 4°. As the wing tested in the present study has an incidence angle less than 4°, the tightly coupled FSI shows a great potential to be employed.

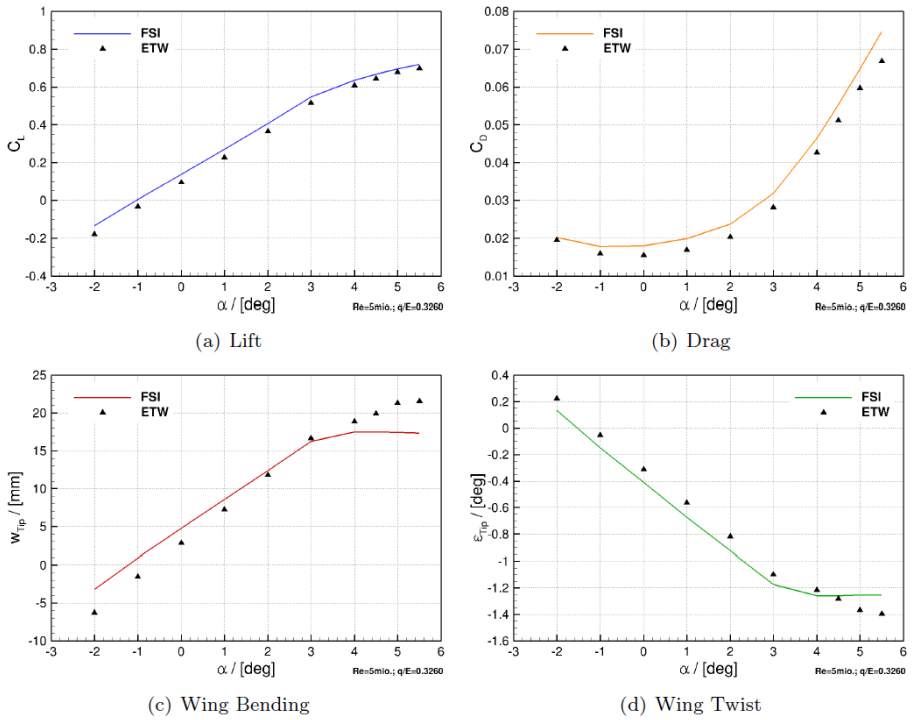

(a) Lift (b) Drag

(c) Wing Bending (d) Wing Twist

Figure 2.6: Validation of the tightly coupled two-way FSI for $Re = 5 \times 10^6$(Keye and Rudnik, 2015)

According to Vrchota et al. (2017), alternative methods to the loosely coupled and tightly coupled two-way FSI have been proposed to compute the geometry deformation. These strategies range in complexity and computational effort. The simplest method consists of measuring the deformation in wind tunnel tests and converting it to the computational model by manually morphing the geometry and the CFD mesh. On the other hand, an intermediate approach, which represents a compromise

between the manual morphing and the two-way FSI, is the use of modal analyses to capture the deformation and correlating it to the CFD simulations (Figure 2.7).

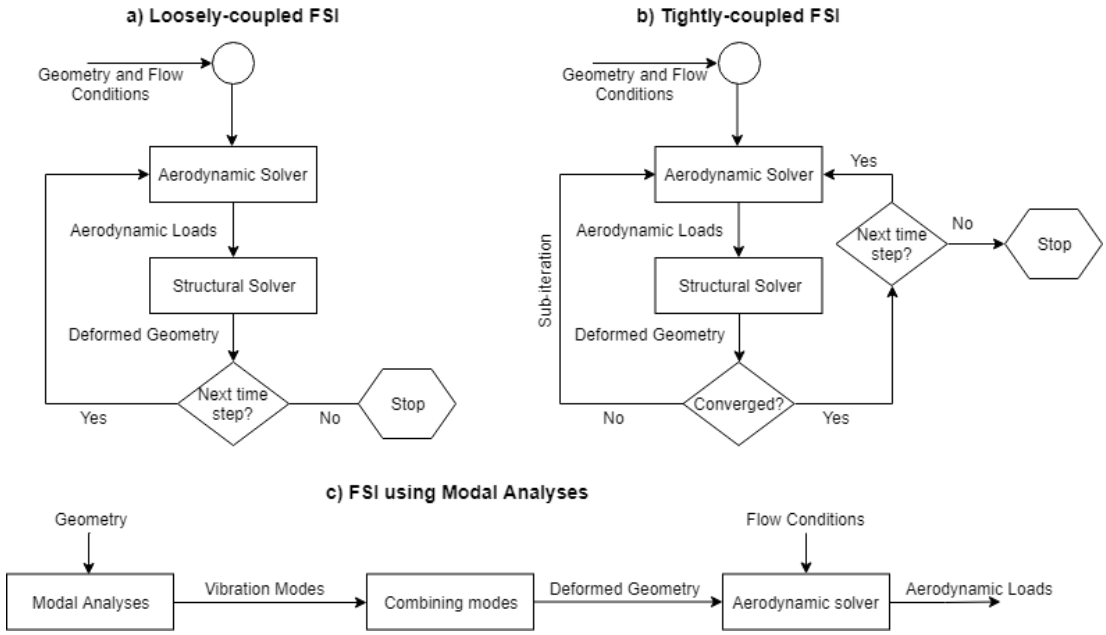

Figure 2.7: Flowchart displaying FSI methods

Vrchota et al. (2017) employed the modal simulations to analyse the implications of wing deformation on the aerodynamic performance of the CRM. For each AoA, the first 20 vibrational modes were computed and the final deformed geometry consisted in a combination of these modes. The aerodynamic analyses were then performed on these deformed shapes and on the rigid wing. In comparison to the CFD results of a rigid geometry, a gain in accuracy to predict the lift and drag coefficient was exhibited when aerodynamic analyses were performed on a deformed wing. For instance, the C_L error decreased from 4.95% to 1.80% at AoA = 0° and Re of 30×10^6. However, the results showed a certain level of disagreement in the bending measurements across the wingspan. For incidence angles of 0° and 3°, an almost constant error of 0.002m and 0.003m was computed, which represents a discrepancy of 25% and 13% at the wing tip. Such errors produced by this method do not have a significant impact on aerodynamic loads of wings operating in free stream, but this method is not suitable for wings in ground effect whose aerodynamic loads are sensitive to the ground clearance.

Eberhardt et al. (2014) performed the blending between numerical models and experiments to analyse the same CRM. At first, the authors observed excessive discrepancies between the results of the CFD model of a rigid wing and the wind tunnel data. They realised this was due to the wing twist. To

rectify the issue, the twist of the wing was measured experimentally and correlated to the numerical model by morphing the geometry. After this process, the error in C_L approximately decreased from 13% to 7% at AoA of 4°. In a following study on the CRM, performed by Yasue and Ueno (2016), a similar methodology was utilised, but the bending measurements of the wing were also included in the morphing process. Eberhardt et al. demonstrated that the model with deformation correction achieved again better agreement with wind tunnel data. For instance, at the $C_L = 0.5$, the drag error decreased from 10% to 5%, and the qualitative correlation of the lift slope was improved as well.

It is evident that the need for collecting experimental data in wind tunnel tests makes this last strategy unfeasible in most applications. Nevertheless, it shows that the model accuracy can be improved by simply computing the static deformation of the wing and transferring it to the CFD simulation. Based on this finding and on the proved efficiency of the loosely-coupled method to determine the wing deflection, a static loosely-coupled simulation is developed and employed in this study.

2.2.2 The significance of Aeroelasticity and its application

Testing either numerically or experimentally the interaction between system dynamics, aerodynamics and structural mechanics has helped engineers and researchers to have a better picture of reality. It not only supported them to detect possible aeroelastic problems, but it also allowed to evaluate design improvements or even to elaborate state-of-the-art concepts.

Inspired by the flight of animals, such dragonflies and hummingbirds, the concept of flapping wings was introduced into Micro Air Vehicles (MAV's), allowing MAV designs to achieve smaller sizes (<15 cm) and slower speeds (<10 m/s). Du and Sun (2010) proved through experiments that the lift generated by flapping wings is mainly influenced by the camber deformation, while the spanwise twist significantly changes the power required for a drone to fly.

In order to further understand this field, Fairuz et al. (2013) conducted numerical and experimental analyses on a flapping wing model. The computational simulation performed in this study consisted of coupling Fluent and ABAQUS in a loosely-coupled FSI strategy. Three different flapping wings were tested at low Reynolds number, a rigid wing, a flexible wing and a highly flexible wing. The results obtained numerically, when validated against the experiments, presented good agreement and proved that the increase of wing flexibility offered beneficial effect to the aerodynamic performance. The lift force peak of the highly flexible wing was 15% higher than the one achieved by the rigid wing. It was also detected that the wind speed and the local camber mainly affected the lift coefficient,

whereas the drag coefficient was predominantly affected by the local angle of attack (geometric twist) – in agreement with the conclusions reached by Du and Sun. All these trends are essential for the development of flapping wings, and new tests can be performed through the use of the FSI model developed in this research.

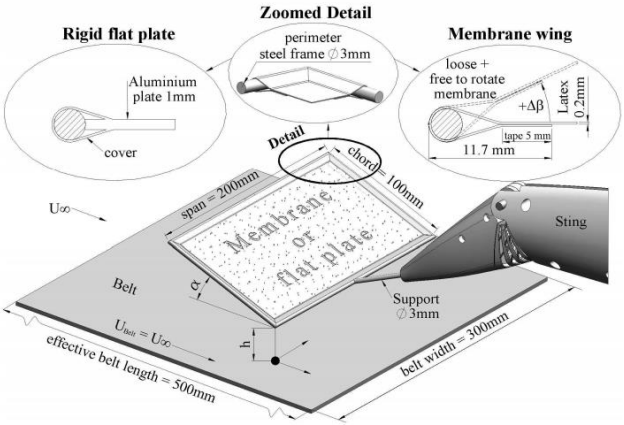

Figure 2.8: Representation of the model used by Bleischwitz (2015)

Membrane wings are another wing concept that can be implemented into MAV's. Shyy et al. (1999) noted that membrane wings provided the following benefits: higher stall angle, greater lift coefficient and more stable response to gust winds. Rojratsirikul et al. (2010) explained that these benefits were due to the body oscillation that energized the boundary layer and produced longer flow attachment. As no research has been previously undertaken to compute the aerodynamic loads of membrane wings in ground effect, Bleischwitz et al. (2015) decided to experimentally investigate this scenario (Figure 2.8). It was observed that, in comparison to the rigid wing, the membrane wing reached higher lift coefficient and stall angle. The authors also verified that the lift increase of a membrane wing was accompanied by a small drag increase, but this drawback did not surpass the overall benefit. The authors pointed out that for angles-of-attack between 0° and 15°, the lift coefficient increased up to 40% (Figure 2.9), whereas the gain in drag coefficient did not exceed 10%. Furthermore, Bleischwitz et al. found out that the membrane and force oscillations had the same frequency but with a phase lag of up to 29°. Therefore, these results highlight the effects that aeroelasticity may have on the lift loss phenomenon of an aerofoil wing.

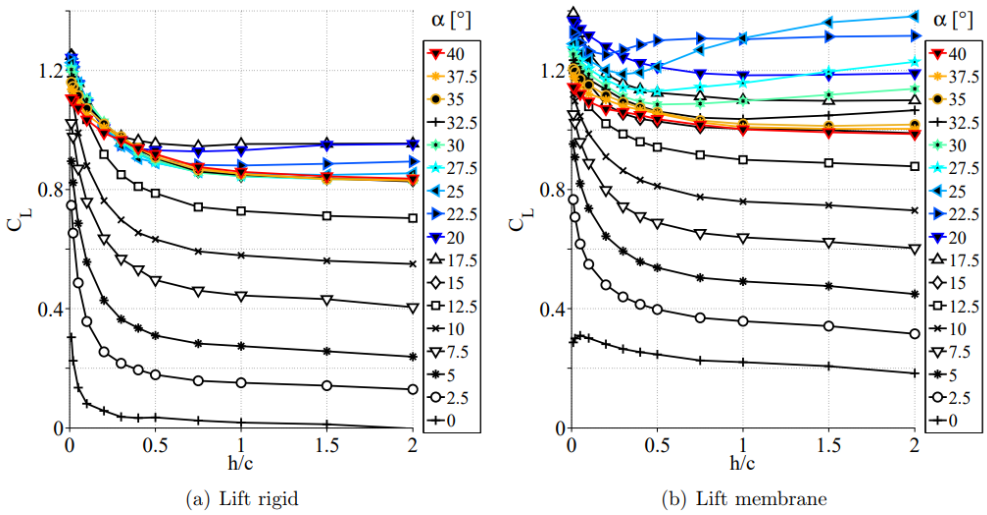

Figure 2.9: Comparison of C_l for a rigid wing and a membrane wing (Bleischwitz et al., 2015)

Inspired by the benefits of membrane wings, Piquee and Breitsamter (2017) tested experimentally and numerically a membrane aerofoil (Figure 2.10). The tests were performed at Reynolds number of 2.8×10^5 for angles of attack varying from 0 to 18°. The computational model consisted of a quasi-2D two-way FSI. The membrane flexibility produced aerodynamic improvements similar to those offered by the camber change in flapping wings. The computational and experimental results showed an increase in lift coefficient and a delay in wing stall from 13° to 15° of angle of attack. The reason for it is the membrane flexibility that allows the aerofoil to adapt its camber with the variation of pressure on its surface and, as result, the boundary layer is maintained attached. Although experiments and simulations exhibited similar trends, the numerical solver overestimated the lift coefficient by approximately 7% and underestimated the drag coefficient by around 40%. This divergence was caused by the 3D effect present in the experiments and missing in the simulations. Thus, qualitative but not quantitative conclusions can be taken from quasi-2D analyses.

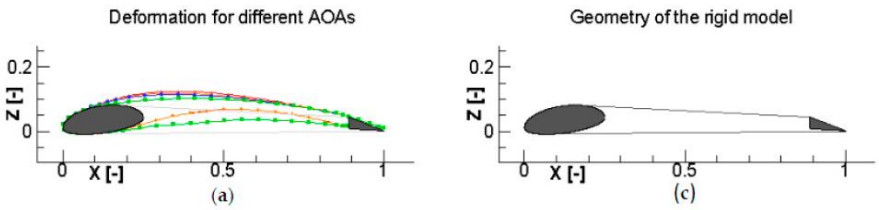

Figure 2.10: Representation of the membrane aerofoil tested by Piquee and Breitsamter (2017)

Wings that adapt themselves, as the concept tested by Piquee and Breitsamter, are defined as morphing wings. Rodriguez (2007) stated that the development of such concept allows engineers to design multi-objective aircrafts since conflicting requirements can be fulfilled by morphing the wing shape for each scenario. Tailoring is one of the morphing techniques based on aeroelasticity, and Shirk et al. (1986) defined it as:

> ‘Aeroelastic tailoring is the embodiment of directional stiffness into an aircraft structural design to control aeroelastic deformation, static or dynamic, in such a fashion as to affect the aerodynamic and structural performance of that aircraft in a beneficial way.’

Based on this strategy, Thuwis et al. (2010) developed a computational framework in order to minimise the induced drag of the rear wing of an F1 car whose aerofoil profile is the BE153-105. This study is the only published work so far to analyse the aeroelastic effects on an F1 vehicle. The optimisation process consisted of changing the wing torsional rigidity by varying the composites lamination parameters and then performing three-dimensional static aeroelastic simulations. The aeroelastic numerical model coupled the commercial Finite Element solver Nastran to the VSAERO CFD solver by following the loosely-coupled FSI strategy. For the optimisation process, a minimum downforce coefficient was set as a constraint, so that the wing produced enough downforce to maintain the car stability during low-speed turns (30 m/s). However, as the velocity increased, the wing twisted and achieved lower drag coefficients, allowing higher top speeds in straights.

Thuwis et al. optimised three cases, where the number of layers for the upper and lower skins varied from 2 to 4. All tests were conducted at a velocity of 92 m/s and at an angle of attack of 10°. The optimisation results showcased that, at this speed, the drag coefficient of the 2 layers and the 4 layers models decreased by 16 % and 10%, respectively, in comparison to an infinitely rigid wing, used as the benchmark.

These studies put in perspective how aeroelastic effects, such as wing oscillation and wing twist, can influence the aerodynamic performance of wings. It is highlighted that no one has ever investigated flexible downforce producing wings in ground effect. The most similar study was undertaken by Bleischwitz et al., but for a membrane wing in ground effect. This knowledge gap brings a wide range of unanswered questions. For instance, the most efficient FSI method to analyse such scenarios is still unknown. To answer this question, the efficiency of the tightly-coupled and the loosely-coupled FSI methods are examined in this work. The tightly-coupled FSI is selected due to its robustness and accuracy, whilst the loosely-coupled FSI is employed because of its simplicity and low computational cost. As previously mentioned, the loosely-coupled is adapted to a static version. Additionally, it is unknown the implications of aeroelasticity on a downforce producing wing. In this chapter, a series of expected implications have been discussed, but the proceeding chapters attempt to prove them.

3. Methodology

3.1 Fluid Mechanics

3.1.1 Governing Equations

ANSYS Fluent 17.2, a commercial computational fluid dynamic (CFD) software, is the platform utilised to solve the fluid motion, which is mathematically represented by the Navier-Stokes equations. These equations are derived from the conservation laws of physics: Conservation of Mass, Conservation of Momentum and Conservation of Energy. As the present study performs all analyses assuming the Newtonian fluid as incompressible, i.e., no variation in density; there is no need to model the conservation of energy. Consequently, only the conservation of mass and momentum are presented. The feasibility of assuming the flow around wings in ground proximity as incompressible for Mach numbers below 0.2 has been proven by Doig et al. (2011).

The conservation of mass or continuity condition states that the rate of change of mass within a fixed volume of fluid is equal to the rate of change of mass flux on the surface of the volume.

$$\frac{\partial \rho}{\partial t} + \frac{\partial (\rho u_i)}{\partial x_i} = 0 \tag{2}$$

Where ρ is the density of the fluid, t is time, u_i represents the velocity components in spatial coordinates x_i. For an incompressible fluid, the density is constant, hence the equation is simplified to:

$$\frac{\partial \mathrm{u_i}}{\partial \mathrm{x_i}} = 0 \tag{3}$$

The conservation of momentum, which is derived from Newton`s second law, expresses that the rate of change of momentum of a fluid particle is equal to the sum of forces on the particle:

$$\frac{\partial (\rho u_i)}{\partial t} + \frac{\partial (\rho u_i u_j)}{\partial x_j} = \frac{\partial \sigma_{ij}}{\partial x_j} + \rho b_i \tag{4}$$

With σ_{ij} representing the Cauchy stress tensor and b_i representing the body forces, such as gravity and buoyancy. For the present study, in which there is no body force, no variation in density and the air is a Newtonian fluid, the equation is resumed to:

$$\frac{\partial (\rho u_i)}{\partial t} + \frac{\partial (\rho u_i u_j)}{\partial x_j} = \frac{\partial}{\partial x_j}\left[\mu\left(\frac{\partial u_i}{\partial x_j} + \frac{\partial u_j}{\partial x_i}\right) - p\delta_{ij}\right] \tag{5}$$

Where p is the fluid pressure, δ_{ij} is the Kronecker delta and μ is the dynamic viscosity of the fluid.

In most of the engineering applications the flow variables do not behave in a smooth, steady and organised manner (laminar), but, instead, they vary in an unsteady and chaotic way (turbulent). The turbulent flow is characterised by rotational structures of different length and time scales. These structures are named eddies and are responsible for dissipating energy. Kolmogorov (1941) described the energy dissipation process as a cascade, in which the energy is gradually transferred from the larger eddies to the smaller ones that are eventually smeared out by the action of viscosity.

In order to investigate the flow turbulence, several methods have been developed, including Direct Numerical Simulation (DNS), Large Eddy Simulation (LES) and Reynolds-averaged Navier-Stokes (RANS). Whereas LES is only capable of solving the larger eddies, DNS is capable of directly solving all turbulence scales. However, employing such methods demands elevated computational resources. On the other hand, RANS models all turbulence structures instead of resolving them, and, as consequence, significantly less computational resources are required to perform it. While DNS and LES were considered for this work, previous studies have demonstrated the RANS model's suitability to predict the flow around wings in ground effect (Diasinos et al., 2014; Keogh et al., 2015; Roberts et al., 2016), justifying its use here.

RANS is based on a decomposition of the flow velocities into a steady mean value (u_i) and a fluctuating term (u_i') for each velocity component:

$$u_i = \bar{u}_i + u_i' \tag{6}$$

Analogously, this is utilised to the flow pressure:

$$p = \bar{p} + p' \tag{7}$$

The RANS equations are derived when this decomposition is applied to the Navier-Stokes equations that are, posteriorly, time-averaged. During this process, six additional non-linear terms rise without any additional transport equations to solve them. These extra terms are called the Reynolds stresses (τ_{ij}) and turbulence models have been developed to further compute them. The turbulence models described here are based on the Boussinesq Hypothesis, which relates the Reynolds stresses to the mean stress rate tensor (τ_{ij}). This relation also implies that the transfer in the turbulent moment is proportional to mean gradients of velocity (Versteeg and Malalasekera, 2007). For scenarios with strong recirculation or separation, this hypothesis is not effective since the stresses are assumed as isotropic.

$$\tau_{ij} = 2\mu_t S_{ij}^* - \frac{2}{3}\rho k \delta_{ij} \tag{8}$$

Where μ_t is the Turbulent Viscosity, S_{ij}^* corresponds to the Mean Strain Rate tensor and k represents the Turbulent Kinetic Energy.

3.1.2 Turbulence Modelling

3.1.2.1 S-A vorticity

The Spalart-Allmaras (S-A) model is a one equation method that solves a modelled transport equation for the turbulent kinetic eddy viscosity (Wilcox, 1993). This method was originally developed by Spalart and Allmaras (1992) to predict the flow over aerofoils in the transonic region, but it also presents robustness to analyse aerofoils in the subsonic regime. The S-A has been shown to be effective to model boundary layers subjected to adverse pressure gradient and suitable to be used with unstructured meshes (Spalart and Allmaras, 1992).

3.1.2.2 k-ε Realizable with the enhanced wall treatment

The k-ε realizable model is a recently new variation of the standard k-ε model, which was initially developed by Chou (1945) and improved by Launder and Spalding (1972). The standard k-ε is a semi-empirical model that uses the exact transport equation for the turbulence kinetic energy (k) and an experimentally based formula for its dissipation (ε) (Launder and Sharma, 1974). This model performs poorly in regions of adverse pressure gradient as well as boundary layer separation (Fluent, 2006). In order to solve these problems, Shih et al. (1995) developed the k-ε realizable model. This model is based on the standard k-ε but presents a new formulation for both eddy viscosity and dissipation rate. With these modifications, the model is capable of better predicting both planar as well as round jets, and it is also expected to exhibit enhanced performance for near wall and swirling flows. Diasinos et al. (2014) has already demonstrated that the k-ε realizable model accurately matched the experiment results of a downforce producing wing in ground effect. Additionally, Diasinos et al. (2014) indicated the necessity of applying specific wall functions, e.g. Low Reynolds or Enhanced Wall Treatment, to better predict flow separation.

3.1.2.3 K-ω Shear Stress Transport (SST)

The k-ω model is a two-equation model based on the model transport equations for turbulent kinetic energy (k) and the specific dissipation rate (ω). The use of the ω term, which is the ratio of ε and k, allows this turbulence model to better predict the flow vortices as well as the boundary layer without requiring a near wall correction. Nevertheless, the k-ω model suffers from high sensitivity to free stream conditions on ω in free-shear flows. In order to correct this issue, Menter (1994) proposed a new formulation for the model. This new formulation, called k-ω SST, consists of a combination between the k-ε and the standard k-ω methods. In free stream and in the outer region of the boundary layer, the flow is modelled with a variant of the k-ε method, and as it reaches the inner region of the boundary layer, the model gradually changes to a modified version of k-ω. Keogh et al. (2015) proved

the effectiveness of this method to investigate the aerodynamic performance of a wing in ground effect.

3.1.2.4 Transition SST

The transition SST model is a-four equation turbulence model that couples two equations from the k-ω SST model with two additional transport equations, one for the intermittency (γ) and the other one for transition onset momentum thickness Reynolds number (Re_θ). The intermittency equation deals with local variables that affect the flow transition and the second additional equation captures the nonlocal influence of the turbulence intensity. Due to these two additional equations, the Transition SST model is capable of computing not only the laminar to turbulent transition region in the boundary layer, but also the reattachment of the flow over aerofoils (Aftab et al. 2016). Furthermore, Aftab et al. (2016) demonstrated that, in comparison to the k-ω SST and k-ε models, the Transition SST method similarly resolved the wake structure.

3.1.3 Numerical Method

The Finite Volume Method is a numerical technique widely used in Computational Fluid Dynamic codes, including Fluent 17.2. This methodology is more deeply described in the textbooks of Versteeg & Malalasekera (2007) and Tu et al. (2018), thereby only an introduction to the topic is presented here. The starting point of the method is to discretise the fluid domain in control volumes or cells. Tu et al. stated that a wide range of cell types – hexahedral, tetrahedral, and polyhedral - can be employed to mesh the flow field. Once the discretisation is finished, the code iteratively solves the integral form of the RANS equations at the cell centre. Solving the integral form of the equations ensures that the flow properties within the fluid domain are conserved. Mesh quality, discretisation algorithms and interpolation schemes of the flow variables are crucial to reach an accurate and stable solution, as it is described in the following sections.

3.1.3.1 Discretisation Schemes

The FVM in Fluent calculates the integral form of RANS equations onto the cell centre. However, to derive the convective terms of these equations, it is necessary to compute the face values. In this study, Upwind discretisation schemes are employed to achieve this. Central differencing schemes are deferred as they are more suitable to analyses with fine meshes and where the effects of diffusion are dominant. Moreover, upwind schemes provide higher transportiveness and account for the direction of the flow, i.e., the face quantities are derived from the cells in the upstream (Versteeg and Malalasekera, 2007).

Fluent provides a number of upwind discretisation algorithms, including the second-order scheme, which is recognised for decreasing the false-diffusion effect. Instead of setting the face value to be equal to the cell-centre value as the first-order scheme does, the second-order algorithm computes the face quantities through a Taylor series expansion from the determined cell-centred solution. This provides better resolution of the flow structures but can rise stability issues, requiring a mesh with improved quality. The second-order upwind scheme has already been used in past numerical simulations of wings by Roberts et al. (2016).

3.1.3.2 Pressure-Velocity Coupling

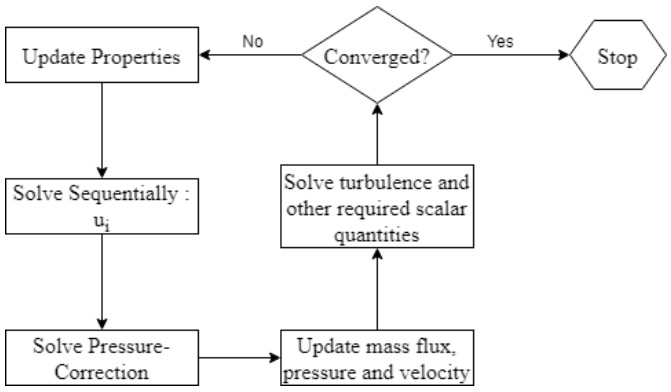

Figure 3.1: SIMPLEC flowchart adapted from Malalasekera and Versteeg (2006)

The SIMPLEC segregated pressure based solver is chosen to iteratively calculate the unknown fluid variables. A segregate algorithm requires less computational memory than a coupled algorithm as the variables are solved and stored individually. The SIMPLEC method was originally developed by Doormal and Raithby (1984) and consists of a modified form of the Semi-Implicit Method for Pressure-Linked Equations (SIMPLE). The difference between these two methods dwells in the way the velocity correction is calculated, and, as result, the SIMPLEC method is able to achieve a converged solution in fewer iterations (Malalasekera and Versteeg, 2006).

3.1.4 Transient Formulation

The transient fluid simulations advance in time through an iterative time-advancement scheme, which is based on a series of sub-iterations per time step, also known as outer iterations. These outer iterations are performed in each time step until the convergence criteria are met and, only after that, the solution progresses in time. The advantage of using the iterative time-advancement scheme is that no splitting error is generated, for additional details see Fluent (2006). To discretise the time derivative of a given fluid property, a first order implicit scheme is utilised (Fluent, 2006). The

implicit scheme provides unconditional stability with respect to time step, giving the user flexibility to determine the desired temporal resolution.

3.2 Solid Mechanics

3.2.1 Governing Equations

The solid mechanic systems obey the same physical laws as fluid systems and they are used to formulate the governing equation of such systems. From the conservation of momentum, the stress equilibrium equation that governs the body deformation is derived:

$$\rho_s \frac{\partial^2 \vartheta_i}{\partial t^2} + \frac{\partial (S_{ji})}{\partial X_j} + f_i = 0 \tag{9}$$

With ϑ_i as the deformation of the body in each Cartesian component, ρ_s representing the density of the solid, f_i as the external load applied and S_{ji} corresponding to the second Piola-Kirschhoff stress tensor, which is calculated as:

$$S_{ji} = 2\mu_S E_{ij} + \lambda_s \delta_{ij} E_{kk} \tag{10}$$

Where E_{ij} is the strain and λ_s and μ_S are the Lame's constants, which are related to the Young's modulus (E_s) and Poisson's ratio ν_s of the material:

$$\lambda_s = \frac{\nu_s E_s}{(1+\nu_s)(1-2\nu_s)} \tag{11}$$

$$\mu_S = \frac{E}{2(1+\nu_s)} \tag{12}$$

3.2.2 Numerical methodology

Similarly to fluid analyses, a numerical method is utilised to solve the governing equations of solid mechanics. ANSYS Mechanical 17.2 simulations are based on the Finite Element Method (FEM). As in the FVM, the FEM subdivides the domain of study in elements or cells, but it differs in how the governing equations are manipulated. Instead of using the strong form of Equation (9), the FEM employs a weak form, i.e., the strong equation is multiplied with a test function (basis function) and integrated. The weak equation is, then, numerically integrated into each element and derived into a system of linear equations, which can be represented in matrix form (Equation 13). These equations are solved in the nodes of each element and interpolated to compute the quantities over the whole element.

$$M_{ij}^s \frac{\partial^2 \vartheta_i}{\partial t^2} + K_{ij}^S \vartheta_i = F_j^s \tag{13}$$

Where M_{ij}^{S} is the mass matrix, F_j^S corresponds to the force vector and K_{ij}^{S} the stiffness matrix. Further description of the FEM can be read in the textbooks of Zienkiewicz et al. (1977) and Schafer (2006).

3.2.2.1 Solution Method

Once the system of linear equations has been set and algebraically manipulated into a matrix, a method is required to solve it. ANSYS Mechanical 17.2 provides direct and iterative solvers. While the first technique finds the solution based on a direct elimination of equations, the second procedure starts by assuming a "guess solution" and iteratively refines it until convergence criteria are reached. Both methods are tested in a statically loaded wing, and, due to the simplicity of the geometry, they have a similar level of accuracy; the direct method, though, is 5% faster. For tightly-coupled FSI analyses, this results in a reasonable reduction in computational resources since more than 2000 structural analyses are performed for a single FSI simulation.

3.2.2.2 Transient Formulation

The time integration in Transient Structural analyses allows FEM to compute the damping and inertia forces of the body. Newmark-beta is the scheme used to time integrate Equation (13). In ANSYS, the Newmark algorithm assumes the acceleration as constant for each time step and derives the displacement and velocity variables from a Taylor series expansion:

$$\vartheta_i^{n+1} = \vartheta_i^n + \Delta t \dot{\vartheta}_i^n + \frac{\Delta t^2}{2}\ddot{\vartheta}_i^n + \beta \Delta t^2 (\ddot{\vartheta}_i^{n+1} - \ddot{\vartheta}_i^n) \tag{14}$$

$$\dot{\vartheta}_i^{n+1} = \dot{\vartheta}_i^n + \Delta t \ddot{\vartheta}_i^n + \gamma \Delta t^2 (\ddot{\vartheta}_i^{n+1} - \ddot{\vartheta}_i^n) \tag{15}$$

Where β and γ are the Newmark integration parameters and determine the method stability. When the acceleration is presumed constant, β and γ are respectively equal to 0.25 and 0.5, providing, thus, unconditional stability for the method.

3.3 Coupling the Structural and the Aerodynamic solvers

The interaction between a flexible body and the fluid domain is a bi-directionally coupled process. The aerodynamic loads are computed by the fluid solver and then transferred to the structural code. The body deformation is, then, calculated and transferred back to the fluid solver. This process occurs in multiple cycles and, as previously mentioned, several numerical methods to perform this coupling have been developed. The interface between the solid domain and the fluid domain is the region where information is transferred. Therefore, it plays an important role in the process. Three conditions, also derived from the laws of physics, rule the Fluid-Structure Interaction problem.

- The geometrical condition declares that the two systems must not overlap and, thus, the fluid and solid domain are continuous.
- The dynamic condition states that the normal forces are balanced on the interface. The force acting on the solid is equal, but in opposite direction, to the force acting on the fluid (Newton's third law).
- The kinematic condition specifies that the fluid and structure velocities on the interface are equal, i.e., the fluid and the solid moves all together at all times.

Approximate solutions of FSI problems do not always comply with these conditions. As previously mentioned, two coupling methods are tested in the present study: the static loosely-coupled FSI and the tightly-coupled FSI, which is described in Section 2.2.1. Whilst a static FSI disregards the dynamic and kinematic conditions as there is no change in physical time, the tightly coupled algorithm presents to be in better agreement with all conditions. Therefore, it is investigated in Section 4.1 how these simplifications impact on the accuracy of the results and on the computational resources required to perform FSI analyses.

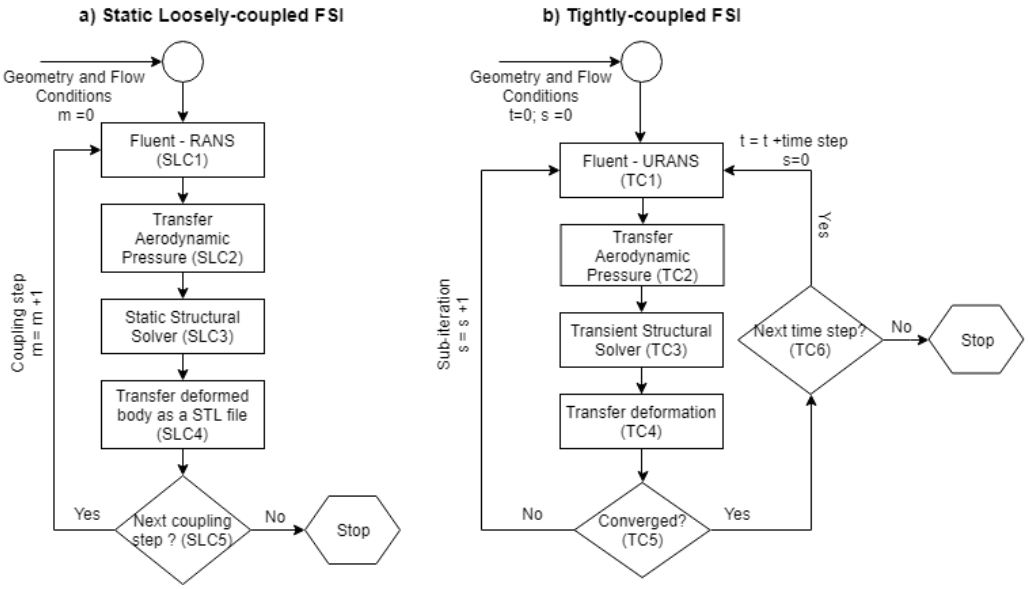

Figure 3.2: FSI Methods – a) Static Loosely-coupled FSI; b)Tightly-coupled FSI

Figure 3.2 displays the process of the tightly coupled FSI and the static loosely-coupled FSI simulations. The tightly coupled analyses are performed using the system coupling built in ANSYS 17.2. This system automatically couples Fluent Unsteady RANS (URANS) simulations (TC1) to transient Mechanical analyses (TC3) and allows these solvers to run sub-iterations in each time step until convergence criteria are reached (TC5). This system simplifies the method in such way that the user only has to deal with the input conditions. On the other hand, the static loosely-coupled approach has been developed during the present study. It consists of running a RANS simulation (SLC1), transferring the aerodynamic pressure

to the Mechanical solver (SLC2), computing the static deformation (SLC3) and, finally, transferring the deformed body as a STL file to Fluent (SLC4). In Fluent the fluid domain is discretised again with the new geometry and the new flow field is predicted (SLC1). The process is repeated in a number of coupling steps (loops) until the convergence criteria are reached (SLC5).

In the static loosely-coupled method developed here, the information transferred between solvers is manually executed by the user (SLC2 and SLC4). This simplifies the strategy but restricts the method performance. The main issue faced is during the process of transferring the aerodynamic pressure from Fluent to ANSYS Mechanical solver (SLC2). During this process, the pressure is always mapped on the initial undeformed geometry (*m=0*) rather than on the deformed geometry of the given coupling step (*m*). It is attempted to map the pressure to the deformed wing, but this does not conserve the elastic properties of the body, i.e., the deformed wing is assumed to have this shape even with no load applied. An alternative solution is considered during the development of the static loosely-coupled method. This solution consists of developing an external code responsible for computing the pressure difference from the given coupling step (*m*) and the previous one (*m-1*). This difference is calculated in each meshing node of the wing and then mapped through an interpolation scheme to the deformed geometry of step *m*. By doing this, the elastic properties are artificially induced to the body. Because this is expected to be more accurate, this strategy will be investigated in future works. During this study (see Section 4.1), it is identified that mapping the aerodynamic pressure to the undeformed wing introduces errors, further increasing the need to consider alternative mapping techniques.

All simulations presented in Section 4.1.1 and 4.1.2, which are used to compare the static loosely-coupled and the tightly coupled FSI methods, are performed on an Amazon Web Service (AWS) machine with 36 3.0 GHz Intel Xeon Platinum CPUs and 72GB DDR4 memory. On the other hand, the analyses of Section 4.2 are conducted on an instance with 4 3.50 GHz Xeon E3-1246 CPUs and 32GB DDR4 memory.

3.3.1 Mesh morphing

Whereas the static loosely-coupled simulations perform a fully re-meshing strategy of the fluid domain to compute the body deformation in each coupling step, the tightly coupled analyses execute a local re-meshing approach. As the tightly coupled algorithm works with a series of inner and outer FSI loops, re-meshing a parcel rather than the entire fluid domain allows a reduction in computational cost.

ANSYS 17.2 allows the user to choose a number of methods to locally update the mesh depending on the characteristics of the simulation. When small displacements compared to the local cell sizes are computed, the smoothing method is employed since it demands less computational resources. On the other hand, the local-remeshing is utilised when large deformations on the geometry are required. This is necessary as the smoothing algorithm deteriorates the cell quality in such scenarios. The switch between methods is based on threshold criteria for skewness and length scales. A deeper description of how each method operates can be found in (Fluent, 2006).

3.3.2 Convergence Criteria

In the static loosely-coupled analyses, it is deemed that the CFD simulations reaches convergence when the continuity and momentum residuals fall to less than 10^{-4} and the force values cease to vary by more than 0.01% for over 1000 iterations. A total of 2500 iterations are needed to reach these criteria. The FSI process itself reaches convergence when the loads change by less than 0.05% between each coupling step.

In the tightly coupled simulations, looser convergence criteria are set for the CFD simulations due to the computational costs of these simulations. Convergence in each time step is deemed when continuity and momentum residuals are respectively below than 10^{-3} and 10^{-4} as well as the force ceases to vary by more than 0.05% between 2 iterations. Furthermore, the change in data transfer values between each coupling step, measured as Root Mean Square (RMS), is set to be less than 10^{-3}. The mathematical formulation of the RMS is found in (Fluent, 2006).

3.4 Model Description

3.4.1 Geometry and Boundary Conditions

The wing analysed in this study is modelled using Creo Parametric 4.0 and matches the model used by Zerihan and Zhang (2000) in his experiments. The span and chord of the wing are 1100mm of and 223.4 mm of chord, respectively. Rectangular shape endplates (100x250mm) are fixed at the tip. The aerofoil profile is the T026 with 3.45° of incidence angle. Similarly to Keogh (2015), a blunt trailing edge of 1.5mm thickness is used. This simplification favours the meshing process by decreasing the skewness angle of the cells in the trailing edge region.

As the numerical model is validated against the experimental tests conducted by Zerihan and Zhang (2000) at the Southampton wind tunnel, the fluid domain is set to match the wind tunnel test-section

size and the initial flow conditions used in the experiments. The wind tunnel has a cross section with maximum dimensions equal to 2.1x1.7m. The outlet and inlet boundaries of the numerical model are extended 7.5c upstream and 15c downstream (Appendix A). A boundary independence study is presented in Section 3.5.1.2, demonstrating that these extensions do not affect the computed aerodynamic forces.

Regarding the boundary conditions, the zero-shear condition is applied for the top wall as it is 1.5m away from the wing, while the lateral wall has a no-slip condition since it is only 0.5m away from the wing tip. The ground across the entire fluid domain is modelled as moving with no-slip condition and velocity equals to the free-stream. The inlet is set with a constant velocity of 30 m/s, turbulence intensity of 0.2% and turbulence length of 0.09m, also matching the experiments conducted by Zerihan and Zhang (2000). The outlet has a constant gauge pressure of 0 Pa and similar turbulence conditions as the inlet. Finally, a symmetry condition is applied to minimise the computational resources required.

For the structural analyses, the wing is positioned in a cantilever configuration. This means that the wing face located on the symmetry plane is fixed without displacement and rotation. The loads are applied through a mapping process, in which the pressure computed in the CFD simulation is transferred to the Mechanical solver and interpolated to the structural mesh.

The wing studied here is made of Acrylonitrile Butadiene Styrene (ABS). Even though airplane and race car wings are made of composites, ABS is selected taking into consideration the low Young's Modulus of this material. This results in higher flexibility and exaggerates the implications of deformation on the aerodynamic performance. Moreover, there is the intention of performing future experimental analyses at Macquarie University, where a wing made of ABS can easily be 3D printed.

3.4.2 Meshing Process

To discretise the fluid domain, a tetrahedral mesh is created in Fluent Meshing 17.2. A structured mesh is not developed as it is not suitable for deforming domains, where cells have to be created, destroyed and/or stretched (Molina et al., 2011). Furthermore, the tetrahedral mesh allows an efficient control of cell sizing in areas where the flow structures are of great importance. To perform such control, three bodies of influence are created. The first one encompassing the zone close to the endplate and the wing. This ensures that the cells nearby the wing do not grow suddenly. The second body of influence between the wing and the ground is created to better capture the influence of the

ground and the flow separation. The third one is positioned behind the wing to improve the wake resolution (Appendix A).

The first layer thickness on the wing and endplate is determined based on the boundary layer theory in flat plates. Fluent (2006) states that the first layer thickness of the mesh should result in a Wall $y+= 1$ in order to ensure the accuracy of the new wall correction model. In Fluent, wall $y+$ is a non-dimensional value dependant on the fluid speed that measures the distance from the wall to the first adjacent mesh centroid (Equation-16).

$$y^+ = \frac{\rho U_\infty y_p}{\mu} \tag{16}$$

Where U_∞ is the free stream velocity and y_p is the first cell centroid height. For simulations with a free-stream velocity of 30 m/s, the calculated first cell centroid height is 0.0111mm, whilst for a velocity of 45 m/s it is 0.0076 mm. Nevertheless, as this formula is developed for flat plates and the object being investigated is a wing, the values are respectively decreased to 0.0075mm and 0.005mm.

The number of inflation layers on the wing and endplate necessary to capture the boundary layer is determined in a similar manner. Firstly, it is calculated the boundary layer thickness for a flat plate (Equation 17), and then using the geometric progression formulation for a series with 1.2 ratio the initial guessed number of layers is determined. After that, contours of eddy viscosity ratio are analysed to verify if the inflation layers capture the total boundary layer thickness. With 26 layers it is possible to meet this last constraint for both Reynolds numbers (4.64×10^5 and 6.96×10^5) tested.

$$\zeta = \frac{0.37l}{Re^{\frac{1}{5}}} \tag{17}$$

For the ground, the last aspect ratio meshing method is used as the cells near the ground drastically change in size throughout the domain. 18 layers are used in the ground with the last aspect ratio of 0.3.

The mechanical mesh is set in order to accurately compute the wing deformation, and the mapping process plays an important role to achieve this goal. This process is highly dependent on the similarity of the mechanical and CFD meshes. Burnett (2016) states that the error when information is transferred decreases if the nodes of both meshes are located in similar positions. Therefore, the mechanical grid is built with tetrahedrals whose sizings are similar to those used on the wing surface of the CFD mesh.

3.5 Validation and Verification

In order to assess the computational model's accuracy and reliability, the American Institute of Aeronautics and Astronautics (AIAA, 1998) advises to conduct a verification and a validation process. These processes are executed in a "building-block" approach (AIAA, 1998), i.e., the fluid dynamics and structural solvers are separately verified and validated. With respect to the validation process, AIAA recommends to undertake it after that the verification is completed. In addition, it is mentioned that the user is required to balance the budgetary constraints and the model's degree of fidelity. Thus, the model does not have to achieve a high-level accuracy when validated against experiments, but rather demonstrate the capability of reproducing the anticipated trends.

3.5.1 Grid Independence Test

The CFD grid independence study is undertaken using the k-ε realizable turbulence model at a constant height of $0.134c$ and Reynolds number of 4.64×10^5 based on a chord length of 223.4mm. Six levels of refinement, ranging from 4.5×10^6 to 1.575×10^7 control volumes, are tested. The aerodynamic loads obtained for each test are compared to that calculated by the finest grid, as advised by AIAA (1998). When subsequent mesh refinement cases do not result in forces varying by more than 1%, it is deemed that the grid refinement has reached convergence.

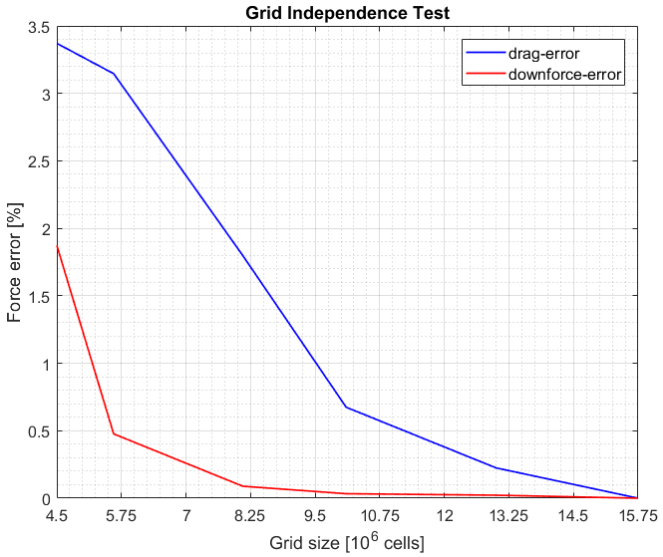

Figure 3.3: Grid Independence Study for CFD mesh

Figure 3.3 demonstrates how the drag and downforce vary for the six grid refinements. It is observed that the maximum variation does not exceed 4% and the convergence criteria for both downforce as well as drag are met with a 10×10^6 elements grid. This mesh provides, thus, a suitable compromise between accuracy and computational cost. The use of the finest mesh is approximately 1.5 times more

expensive and does not lead to large benefits in loads accuracy or better resolution in flow structures. Following the formulation of Celik and Zhang (1995) to determine the Grid Convergence Index (GCI) error, it is calculated that the downforce and drag GCI errors, when comparing the 10×10^6 elements mesh to the 1.575×10^7 cells grid, are respectively 0.07% and 1.41%.

For the mechanical mesh, 5 grid refinement levels are tested. The number of nodes ranges from 4.6×10^4 to 1.9×10^5. No mesh with nodes count below 1.9×10^5 is considered because they either introduce an error when mapping the aerodynamic pressure or they do not properly discretise the geometry, i.e., the aerofoil profile is not preserved. In the static loosely-coupled FSI, it is important to preserve the aerofoil shape since the deformed Mechanical domain works as the geometry input for a following Fluent simulation (SLC4). All simulations are performed with the pressure measurements calculated by the 10×10^6 cells CFD mesh. The displacements at the bottom tip of the wing computed by all meshes are compared and, due to the simplicity of the geometry, the coarsest mesh deflection only differs by 0.6% in comparison to the finest mesh. Therefore, the mesh with 1.9×10^5 nodes is selected for future simulations.

3.5.2 Boundary Position Test

The position of the inlet and outlet boundaries are varied separately in order to ensure that they are not affecting the numerical solution. No adjustment is done for the top and side walls as they match the dimensions of the wind tunnel used in Zerihan's experiments (Zerihan and Zhang, 2000). The baseline positions are set as $7.5c$ upstream and $15c$ downstream, taking as reference the leading edge. The boundary dependency study is performed with increments of $2.5c$ for both the inlet and the outlet.

The collected data from the simulations showcases that the downforce and drag coefficients vary by 0.31% and 0.44%, respectively, when the inlet is extended to $15c$ upstream. On the other hand, the changes in aerodynamic coefficients due to positioning the outlet boundary at $22.5c$ downstream are not greater than 0.01%, Therefore, the baseline extensions are considered suitable for the following studies as the impact of enlarging the fluid domain is negligible.

3.5.3 Validation

3.5.3.1 CFD Validation

Four different turbulence models that have already been used in numerical simulations of wings in ground effect are tested here in order to assess how they predict the aerodynamic forces of Zerihan's

wing. The simulations using the Spalart-Allmaras, k-ε realizable, k-ω SST and Transition SST turbulence models are conducted at a ground clearance of $0.134c$ and Reynolds number of 4.64×10^5.

Figure 3.4 and 3.5 show that all turbulence models overpredict drag and underpredict downforce generated by the wing. However, the Transition SST presents the best correlation to the experiments. With regards to downforce accuracy, the Transition SST is followed by k-ε realizable and S-A, whereas in terms of drag, it is followed by k-ω and S-A models. As k-ω exhibits the largest downforce inaccuracy, and this is the main aerodynamic load to deform the wing, following analyses using this model are discarded. The use of the Transition SST is also rejected since it is not as computationally efficient as the k-ε realizable and the S-A models. In comparison to the computational time spent by the S-A model, the Transition SST takes approximately 3.2 times more to achieve the solution, whilst the k-ε realizable takes 1.75 times. The gain in accuracy when using the Transition SST does not justify the increase in computational cost.

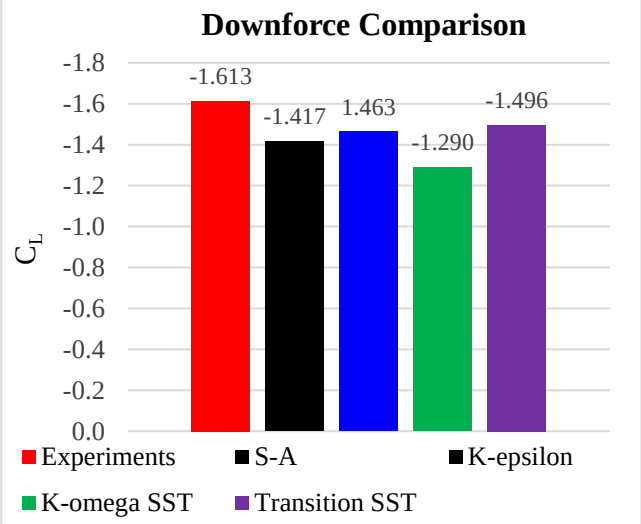

Figure 3.4: Turbulence Models Comparison of C_L

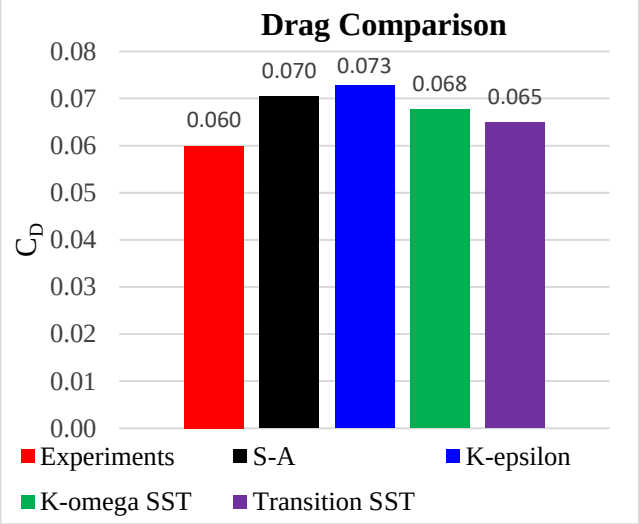

Figure 3.5: Turbulence Models Comparison of C_D

From Figure 3.6, it is seen that k-ε realizable model captures the critical height at 0.080c, matching the experimental results within an absolute error of $0.002c$ or a relative error of 2.44%, whereas the S-A predicts the critical height at 0.091c, an error of 10.98%. Furthermore, in comparison to the downforce measurement achieved by the experiments, the k-ε realizable presents better quantitative agreement than the S-A model. The k-ε realizable more accurately reproduces the loss in downforce with reductions in ground clearance and reduces the maximum error in downforce by 1.79%. In general, an adequate quantitative agreement is found between the numerical simulations with the k-ε realizable model and the experiments. The maximum error in downforce is -9.42% at $h/c = 0.112$. With respect to drag, the S-A model on average decreases the error by 4%, but as already mentioned,

the main concern is the degree of accuracy in downforce. Therefore, the computational model using the k-ε realizable is selected for the following simulations. It not only reproduces the trends noticed in the experiments, which is the main requirement of the validation process but also computes the loads with an adequate accuracy. The aerodynamic loads, specifically the lift, will be the most critical factors to determine the correct deformation that the wing will experience.

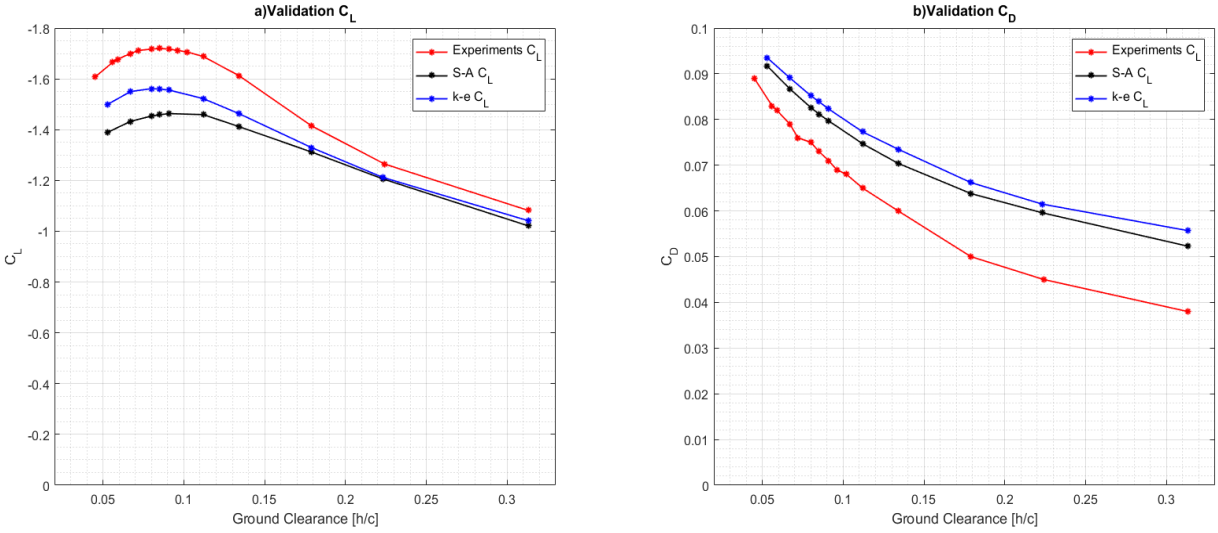

Figure 3.6: CFD validation

3.5.3.2 Mechanical Solver Validation

As the wing is fixed in a cantilever configuration, the maximum deflection computed by the Mechanical solver is validated against the analytical solution to calculate the maximum deflection of a cantilever beam. The analytical solution is given by Equation (18) (Beer et al., 2001). The validation is performed by applying vertical loads ranging from 50N to 300N, and it is seen that the Mechanical solver well reproduces the linear relationship between load and deflection with an angular coefficient error of 1.48% (Appendix D). The angular coefficient of the analytical solution is given by $\frac{l^3}{3E_sI}$, while for the numerical solutions it is calculated by Equation (19).

$$\vartheta = \frac{Fl^3}{3E_sI} \tag{18}$$

Where F represents the applied load, l is half of the wingspan and I is the second moment of inertia.

$$m = \frac{\vartheta_{P_2} - \vartheta_{P_1}}{F_2 - F_1} \tag{19}$$

Where ϑ_{P_2} and ϑ_{P_1} are the deflection measurements when loads F_2(300N) and F_1(50N) are applied.

4. Results

4.1 Coupling methods

In order to select the most suitable coupling method, aeroelastic analyses of the wing model are conducted using the static loosely-coupled and the Tightly-Coupled methods. These simulations are performed at ground clearances of $0.112c$ and $0.134c$ at Reynolds number of 4.64×10^5. Wing deformation, aerodynamic loads, flow structures and computational time are compared to investigate how both methods differ. Three reference points are used to measure the wing deflection (Figure 4.1 and Table 4.1). Points A and B are respectively located in the leading and trailing edge and are used to calculate the wing twist. Point C is positioned on the bottom surface of the wing tip and works as the wing deflection reference.

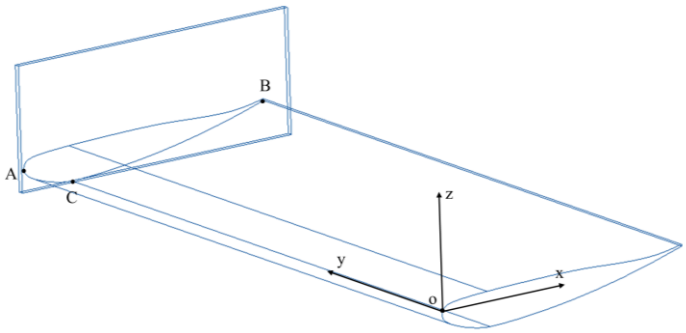

Figure 4.1: Point Locations

Point	x-coordinate (mm)	z-coordinate (mm)
A	0	0
B	223.2	12.6
C	44	-18.2

Table 4.1: Point Locations (mm) taking as reference the leading edge

4.1.1 Tightly coupled FSI

Tightly-coupled simulations are solved with $\Delta t = 0.001s$ for a total real time of $1.725s$. 1725 time steps present to be adequate to capture a stable oscillation in deflection and in force values. The results show that the values of the last three oscillation peaks do not change by more than 0.1% for the aerodynamic forces and by more than 2% for the deflection measurements. Furthermore, solving the simulations for a longer time results in no change to the mean downforce, drag, deflection and wing twist measurements.

At the beginning of the simulation, large oscillations are observed but they tend to quickly dampen out, especially when the wing is positioned at $h = 0.134c$. Figure 4.2 shows that in the last three oscillation cycles of the $h = 0.112c$ simulation, the downforce maximally oscillates by +/-1.10%, the drag by +/-2.53%, and the deflection by +/-25.18%. On the other hand, at $0.134c$, the downforce,

drag and deflection have a maximum variation of +/-0.40%, +/-0.92% and +/- 12.25%, respectively. No effective change in angle of attack due to aeroelasticity is revealed for any of the tests, as consequence, no further details are given in respect to this parameter. These results indicate that dynamic flutter is not likely to happen in the conditions tested here, but the increase in oscillations amplitude from the $h = 0.134c$ to the $h = 0.112c$ suggests that stall flutter may happen when the wing is positioned closer or at the critical height. Table 4.2 presents the maximum and minimum values computed for C_L, C_D and deflection in the last complete oscillation cycle (from 1.670s to 1.707s) as well as an average value of the last four cycles.

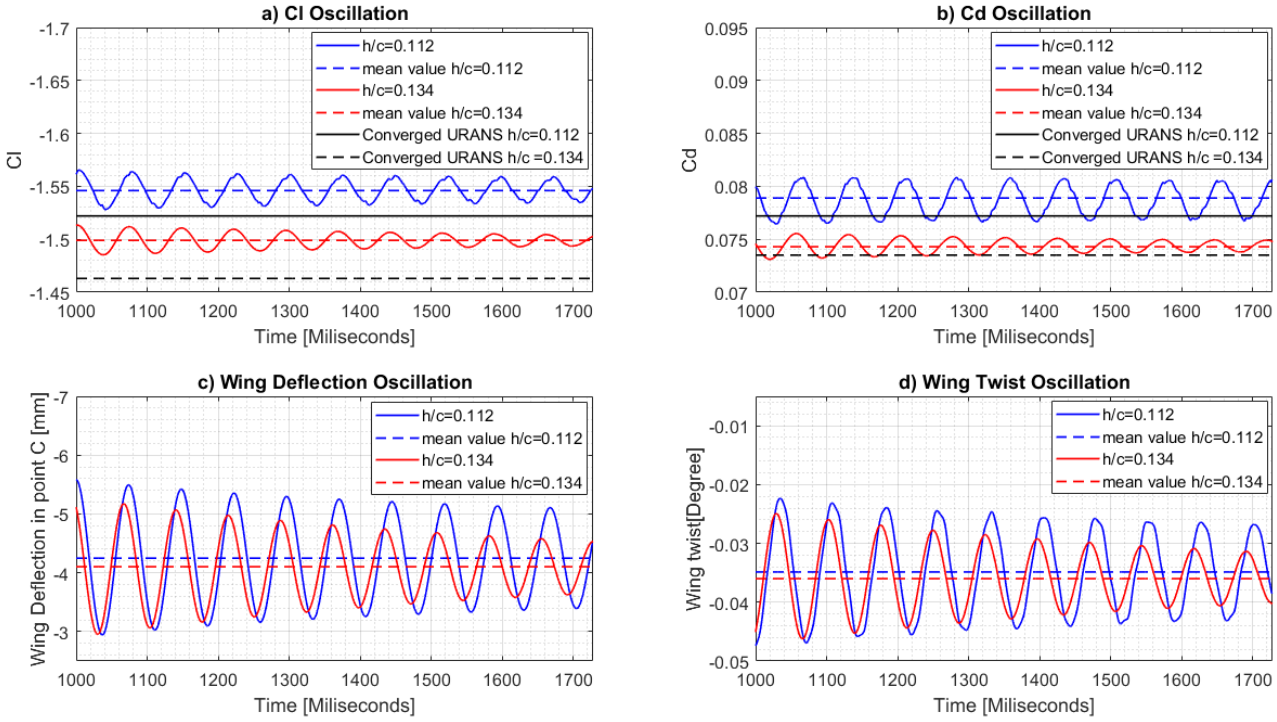

Figure 4.2: Oscillation of aerodynamic loads, deflection and wing twist

	$h = 0.112c$	$h = 0.134c$
C_L Peak / Valley	-1.563/ -1.537	-1.504 /- 1.493
C_D Peak / Valley	0.0809/ 0.0774	0.0750/ 0.0738
Deflection Peak /Valley (mm)	-5.17/ -3.33	-4.58/-3.63
Average C_L	-1.546	-1.499
Average C_D	0.0789	0.0743
Average Deflection (mm)	4.25	4.08

Table 4.2: Tightly-coupled FSI measurements

Unsteady RANS (URANS) simulations of a rigid wing are performed in order to ensure that the observed loads oscillations are a result of the aeroelastic effects and not caused by the transient nature of the simulation. URANS analyses are performed with the same time step size (Δt) used in the tightly-coupled simulations. The results achieved by this methodology indicate that there are no oscillations in the aerodynamic forces for a rigid wing and, in comparison to the RANS simulations, the forces maximally differ by 0.39%. Therefore, it is concluded that the wing aeroelasticity is not only responsible for causing the load oscillations, but also for increasing their mean values.

	$h = 0.112c$		$h = 0.134c$	
	C_L	C_D	C_L	C_D
Rigid wing - RANS	-1.5220	0.0774	-1.463	0.0737
Rigid - URANS	-1.5280	0.0772	-1.467	0.0735
Difference RANS-URANS	0.39%	-0.25%	0.27%	-0.27%
Tightly-coupled FSI - Average	-1.546	0.0789	-1.499	0.0743
Difference RANS-FSI	1.58%	1.94%	2.46%	0.81%

Table 4.3: Force coefficients computed by rigid wing-RANS, rigid wing - URANS and flexible wing - Tightly-coupled FSI

A Fast Fourier Transform is performed and showcases that downforce, drag and deflection oscillate with the same frequency (Table 4.4). This is consistent with the data collected by Bleischwitz et. al. (2015) and Molina and Zhang (2011). Additionally, the FFT calculates secondary oscillation modes when the wing is positioned at $h = 0.112c$. These modes have frequency superior to 40 Hz and amplitudes 12.2 times smaller than the main oscillation. The vortex starting to breakdown is expected to be the reason for these secondary modes since they are not observed at $h = 0.134c$.

Molina and Zhang (2011) indicated that low heaving frequencies ($f_n < 0.55$) do not produce any added-mass effect nor any significative change in the effective incidence angle. This suggests, thus, that the benefits of using transient simulations are minimal and, as consequence, static loosely-coupled FSI simulations are suitable to investigate the aeroelastic behaviour of wings in ground effect.

The FFT is used once more to inspect if there is any time delay, also known as hysteresis, between the forces and deflection oscillations. This behaviour has already been noticed by Bleischwtiz et al. and Molina et al. (2011). Table 4.3 displays that the downforce oscillates with a time delay around 4 and 5 milliseconds in respect to the deflection, whereas the drag peak/minimum happens between 10 and 11 milliseconds earlier than the deflection peak/minimum. The time-delay between deflection

and downforce is a result of the flow development after that the geometry deforms, whilst the phase advancement in drag suggests a combination of different factors. The vortex oscillation, changes in the wake structure and/or the velocity in which the body deforms are investigated to detect the reason for this drag advancement. However, it has not been possible to determine the exact cause since the variation in drag during these 10 to 11 milliseconds does not exceed 0.04N and the consequences of such variation are imperceptible. Therefore, it is suggested to perform future studies with lower torsional and bending stiffness in order to maximize the implications of aeroelasticity.

	$h = 0.112c$	$h = 0.134c$
Frequency (Hz)	13.31	13.69
Normalised Frequency (f_n)	0.311	0.3203
Period (s)	0.0751	0.0730
Deflection-Downforce Delay(ms)	5	4
Deflection-Drag Delay (ms)	-11	-10

Table 4.4: Transient characteristics of oscillations

The flow structures computed by the tightly-coupled FSI are only displayed in the following section when both FSI methods are compared among themselves and to the RANS simulations of a rigid wing.

4.1.2 Static Loosely-coupled FSI

Table 4.5 shows the behaviour of aerodynamic forces and deflection measurements throughout the loops of static loosely-coupled FSI simulations. In only three coupling steps the simulations achieve a converged value. From the second to the third coupling step the lift coefficients and deflection change respectively by no more than 0.13% and 0.08%, while the C_D and twist have no significant variation.

No significant variation in angle of attack is evident using the static loosely-coupled method, which is consistent with the results of the tightly-coupled method. Moreover, the comparison of the rigid wing and the flexible wing reveals that deformation leads to higher downforce and drag. At $h = 0.112c$, the downforce changes from -1.526 to -1.543, whilst the drag coefficient raises from 0.0774 to 0.0785, a respective gain of 1.11% and 1.42%. At $h = 0.134c$, the C_L varies from -1.463 to -1.488, while the C_D increases from 0.0735 to 0.0738, a respective increment of 1.71% and 0.41%.

Coupling Step	$h = 0.112c$							
	C_L	ΔC_l per step	C_D	ΔC_D per step	Deflection (mm)	$\Delta Deflection$ per step	Twist (°)	$\Delta Twist$ per step
1	-1.526	-	0.0774	-	-4.132	-	-0.0351	-
2	-1.545	1.25%	0.0785	1.42%	-4.145	0.31%	-0.0346	-1.42%
3	-1.543	-0.13%	0.0785	0.00%	-4.143	-0.05%	-0.0346	0.00%
-	$h = 0.134c$							
1	-1.463	-	0.0735	-	-3.975	-	-0.0356	-
2	-1.489	1.77%	0.0738	0.41%	-3.993	0.45%	-0.0356	0.00%
3	-1.488	0.07%	0.0738	0.00%	-3.990	-0.08%	-0.0356	0.00%

Table 4.5 : Masurements througout coupling steps

Table 4.5 indicates that the deflection does not vary at the same rate of downforce in each coupling step, contradicting the linear relationship detected in Section 3.5.3.2. In the second coupling step, at $h = 0.112c$, the downforce increases by 1.25%, whereas the deflection only enhances by 0.31%. At $h = 0.134c$, the gain in downforce is approximately 1.77%, while the increment in deflection is 0.45%. Such trend is not witnessed in the third coupling step as all parameters change in similar proportion.

A variation in the y-position of the Centre of Pressure (CoP) towards the symmetry plane can explain why the downforce and deflection do not have a linear dependency. A proportional relationship between loads and body deformation is only expected when the load application point is invariable. The simplest way to determine changes in the CoP y-position consists of measuring the resultant moment in the x-direction (M_x). If M_x increases at a reduced rate than downforce, it suggests that the CoP has an inboard movement. However, Table 4.6 demonstrates that M_x increases at a slightly higher rate than downforce, indicating that the CoP is actually moving towards the endplate.

Coupling Step	$h = 0.112c$				$h = 0.134c$			
	M_x (N.m)	ΔM_x per step	C_L	ΔC_L per step	M_x (N.m)	ΔM_x per step	C_L	ΔC_L per step
1	-23.85	-	-1.526	-	-23.00	-	-1.463	-
2	-24.23	1.59%	-1.545	1.25%	-23.32	1.39%	-1.489	1.77%
3	-24.24	0.04%	-1.543	-0.13%	-23.34	0.09%	-1.488	0.07%

Table 4.6: M_z computed in each coupling step

The accuracy of transferring the loads from CFD to the Mechanical solver is examined to verify if this is the cause for the deflection inconsistency. In the first step, when the wing is rigid, the downforce computed by the CFD solver and the downforce mapped to the Structural solver maximally differ by 0.221%. For the second and third steps, the maximum error amplifies to 1.159% (Table 4.7). This indicates that approximately only 0.3% of the increment in downforce is transferred to the Mechanical solver, explaining the inconsistent deflection behaviour. The reason for this mapping error is the process chosen to transfer the aerodynamic pressure (Section 3.3) since the pressure is always mapped to the rigid wing (initial geometry of the simulation). As the mesh nodes of mechanical mesh and the CFD mesh are not identical, a mapping error is introduced. It is also concluded that, in the first coupling step, the difference in forces is a result of the mapping interpolation process rather than a mapping error since the CFD geometry input is still the undeformed wing.

	$h = 0.112c$	$h = 0.134c$
Coupling step	Error between forces in CFD and Mechanical Solver	
1	-0.171%	-0.221%
2	-1.043%	-1.159%
3	-1.043%	-1.037%

Table 4.7: Mapping and Forces error

Further analyses demonstrate that, for the range of deflections tested, the mapping error and the wing deflection have an almost linear relationship (Appendix E). For the maximum deflection analysed, 10 mm, the maximum error is 2.78%. As the increment in deflection is supposed to be proportional to the gain in downforce, a difference of 2.78% in forces leads to an error of 0.278 mm (2.78% of 10mm). Assuming that the opposite feedback is also linear, i.e., an increase/decrease in deflection is followed by a proportional raise/loss in downforce, this 0.278mm error produces a change in C_L that does not surpass 0.12%[*]. To ensure that this error is irrelevant and the static loosely-coupled method is indeed feasible, the results achieved by both FSI methodologies are compared. It is important to mention that the tightly coupled FSI does not present the same mapping issue since the aerodynamic loads are mapped to the deformed wing of the respective coupling time step.

By comparing the results achieved by the static loosely-coupled and the tightly-coupled FSI (Table 4.8), it is revealed that the mapping problem does not raise large disagreements between the two

[*] Calculation taking into consideration that, for the $0.134c$, a deflection of 3.99mm results in 1.73% gain in downforce

methods. Even though the static loosely-coupled does not capture the wing oscillation, it accurately computes the time-averaged aerodynamic coefficients and wing deflection. The maximum difference in forces does not exceed 0.73%, whilst the maximum deflection discrepancy is 2.59%. Moreover, the comparison of the computational resources indicates that the tightly coupled FSI requires more than 157 hours, whereas the static loosely coupled FSI demands approximately 21 times. Thus, it is unfeasible to employ the tightly-coupled method to simulate a wide range of scenarios.

	$h = 0.112c$			$h = 0.134c$		
	Tightly coupled	Loosely Coupled	Difference	Tightly coupled	Loosely Coupled	Difference
C_L	-1.546	-1.543	-0.20%	-1.499	-1.488	-0.73%
C_D	0.0789	0.0785	-0.52%	0.0743	0.0738	-0.67%
Deflection (mm)	-4.25	-4.14	-2.59%	-4.08	-3.99	-2.21%
Computational Time (Hours)	157.27	7.48	2102%	165.34	7.51	2277%

Table 4.8: Results achieved by the tightly coupled and the static loosely-coupled FSI methods

In order to examine the feasibility of the static loosely-coupled FSI in reproducing trends generated by wing aeroelasticity, the flow structures computed by both FSI simulations are compared to those captured by RANS simulations of a rigid wing. Pressure coefficient plots, which are collected at $1/4c$ downstream of the leading edge, wall-shear stress and vorticity contours are the main parameters analysed. As both cases, $h = 0.112c$ and $h = 0.134c$, have similar trends, only the results associated to the $h = 0.112c$ are presented. The plots of the tightly-coupled FSI are taken at $1.670s$ (maximum deflection point) and $1.707s$ (minimum deflection point).

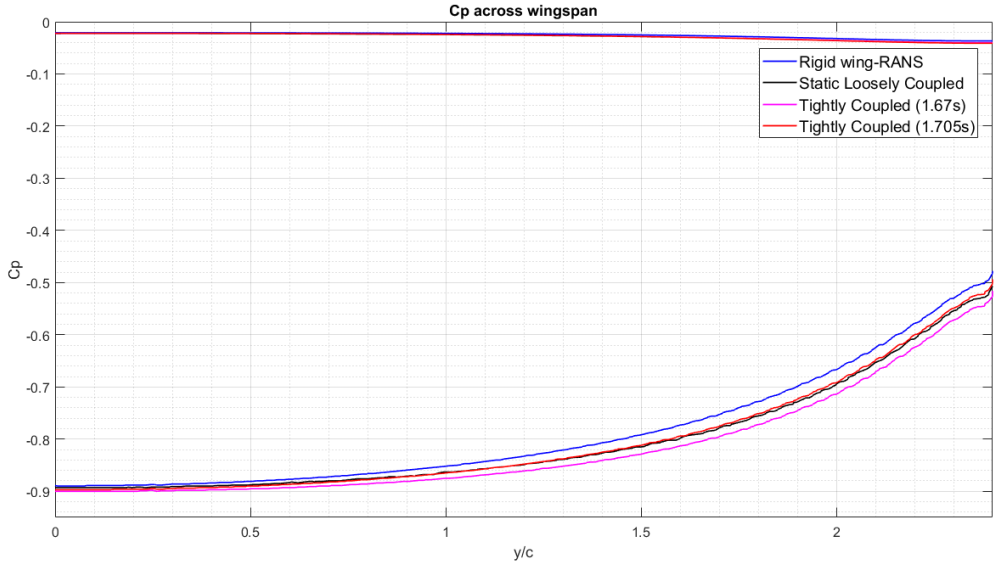

Figure 4.3 : Pressure Coefficient at $x = 1/4c$ for different FSI methods

Figure 4.3 shows that all simulations compute similar values of Cp, especially at $y = 0$, where the wing is fixed. Close to the tip ($y = 2.4c$), the Cp increases due to the airflow leakage from the high-pressure region to the low-pressure region (Mcbeath 1998). However, it is noticed that the deformation reduces the suction loss. For the cases tested so far, the largest deflection leads to the lowest suction loss, which is observed in the tightly coupled FSI at 1.670s. The static loosely-coupled simulation gauges Cp values that lay in between the minimum and maximum deflection, being closer to the minimum deflection (tightly-coupled at 1.707s). This is consistent with the downforce measurements as the C_L computed by the static loosely-coupled is also slightly closer to the 1.707s case.

Wall shear plots are used to indicate the regions in which flow separates. By overlaying the shear stress plots computed by the numerical model and the flow visualization acquired on the experiments of Zerihan and Zhang (2000), it is possible to determine a shear stress reference value that reveals the flow separation regions (Diasinos et al. 2011). In the present study, wall shear stress less than 1 represents these regions (Appendix F)

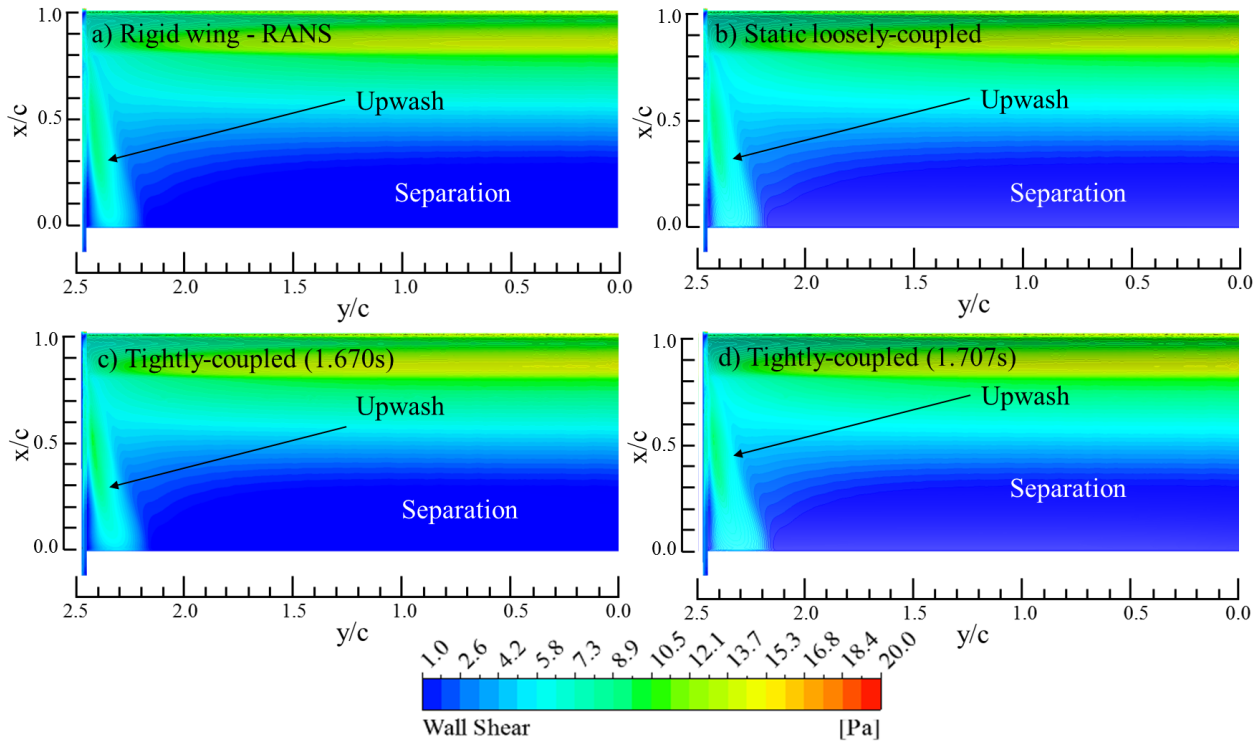

Figure 4.4: Wall-shear stress contours - a) Rigid wing - RANS; b) Static loosely-coupled FSI; c) Tightly-coupled FSI (1.670s); d) Tightly-coupled FSI (1.707s). Flow direction: from top to bottom of the page.

It is exhibited in Figure 4.4 that both FSI methods are able to compute the separation and upwash regions. Due to wing deformation, the upwash becomes wider and the separation is intensified. The

comparison of the two time frames of the tightly coupled FSI shows that when the wing reaches its maximum deflection, the separation is the greatest.

The comparison of vorticity contours taken 1.25c downstream of the leading edge showcases that all simulations compute the core of the main tip vortex in a similar location (Figure 4.5). Furthermore, both FSI methodologies are able to demonstrate the enlargement in vortex size as a result of aeroelasticity. It is also observed that the maximum wing deflection generates the largest increase in vortex width. The static loosely coupled FSI presents an average result of the 1.707s and 1.670s time frames.

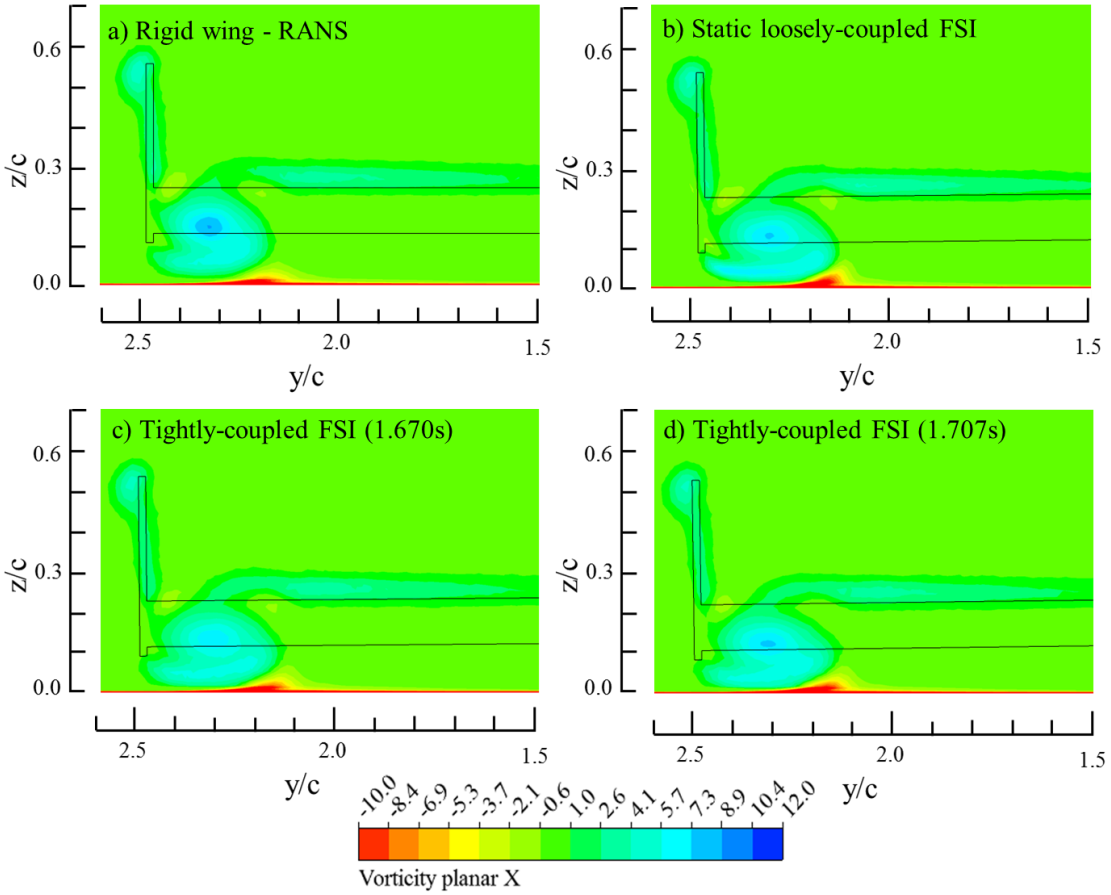

Figure 4.5: Vorticity planar contours - a) Tightly-coupled FSI (1.670s); b) Tightly-coupled FSI (1.707s); c) RANS (rigid wing); d) Static loosely-coupled FSI. Flow direction: into the page.

All results indicate that the static-loosely coupled FSI is not only a feasible strategy to analyse the time-averaged implications of aeroelasticity on a wing in ground effect, but also the most efficient. It accurately computes the average aerodynamic loads and deflection measurements as well as resolves the variations in flow structures due to aeroelasticity. In addition to it, this method requires significantly less computational resources, achieving the results 21 times faster.

4.2 The aeroelasticity impact on wings in ground effect

It is analysed how the lift loss phenomenon of a rigid wing and a flexible wing differ. The static loosely-coupled FSI methodology is employed to perform the analyses for ground clearances ranging from $0.053c$ to $0.313c$ at Reynolds number of 4.64×10^5 and 6.96×10^5. The Re varies by changing the velocity inlet and the ground moving speed so that the physical condition near the ground is consistent for all simulations. As previously mentioned, the first cell height is adapted so that the wall y+ does not exceed 1.

The implications of Reynolds number on the lift loss phenomenon of a rigid wing are investigated. It is observed that the critical height does not vary with the Reynolds number tested. However, due to the higher Reynolds number, the downforce augments by 1.35% to 2.6%, while the drag coefficients decrease by 2.3% to 3.5%. This trend is in quantitative agreement with the results achieved by Doig et al. (2011).

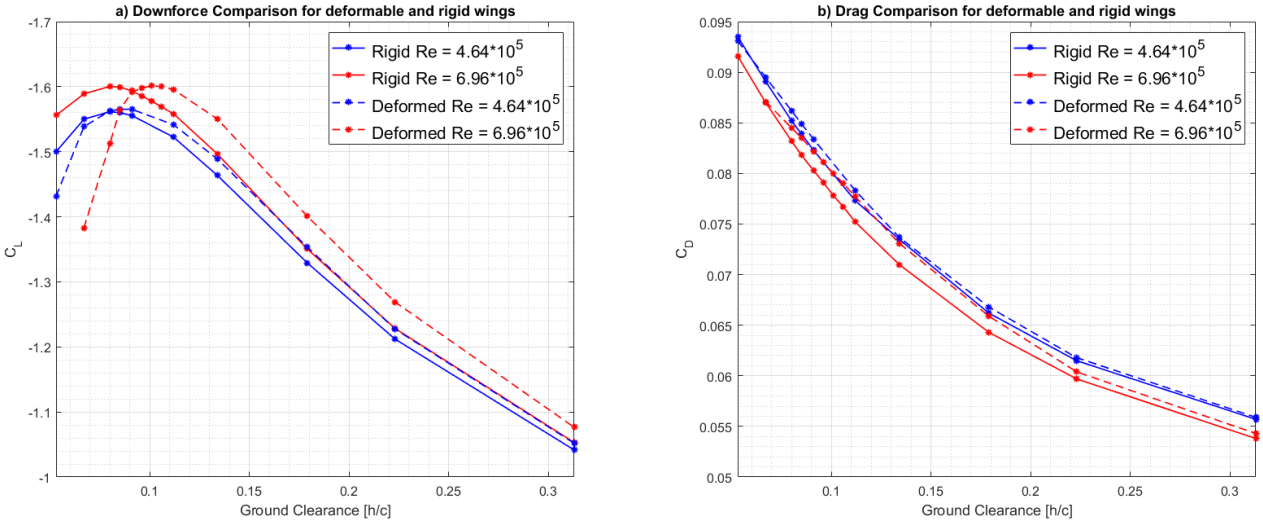

Figure 4.6: Aerodynamic loads comparison of rigid and flexible wings at Reynolds number of 4.64×10^5 and 6.96×10^5[†]

After processing the static loosely-coupled FSI, it is seen in Figure 4.6 that the wing deformation does affect the lift loss phenomenon for both Reynolds number tested. The impact, however, is larger for the higher Re cases since the magnitude of the aerodynamic forces is greater and, as result, the aeroelastic implications are more evident. While for the lower Re the critical height shifts from $0.080c$ to $0.091c$, it varies from $0.080c$ to $0.101c$ for the higher Re.

[†] No aeroelastic analysis was conducted at $0.053c$ for Reynolds number of 6.96×10^5 as the distance from the endplate to the ground was less than 2 mm, and the inflation layers could not be generated in this region.

Figure 4.7 displays the variation in wing deflection and twist for different ground clearances. Even though minimal changes in AoA are observed, the results suggest that the wing is experiencing a wash-out effect (reduction in incidence angle) as result of the downstream movement of the Centre of Pressure (CoP) position. On the other hand, the wing deflection presents to be strictly dependant on the downforce measurements, which is consistent with all results seen so far. The maximum deflections at both Reynolds number happen at the same heights in which the downforce is maximum. Therefore, it is concluded that the changes in the lift loss phenomenon are related to the wing deflection, but not to the variation in the angle of attack.

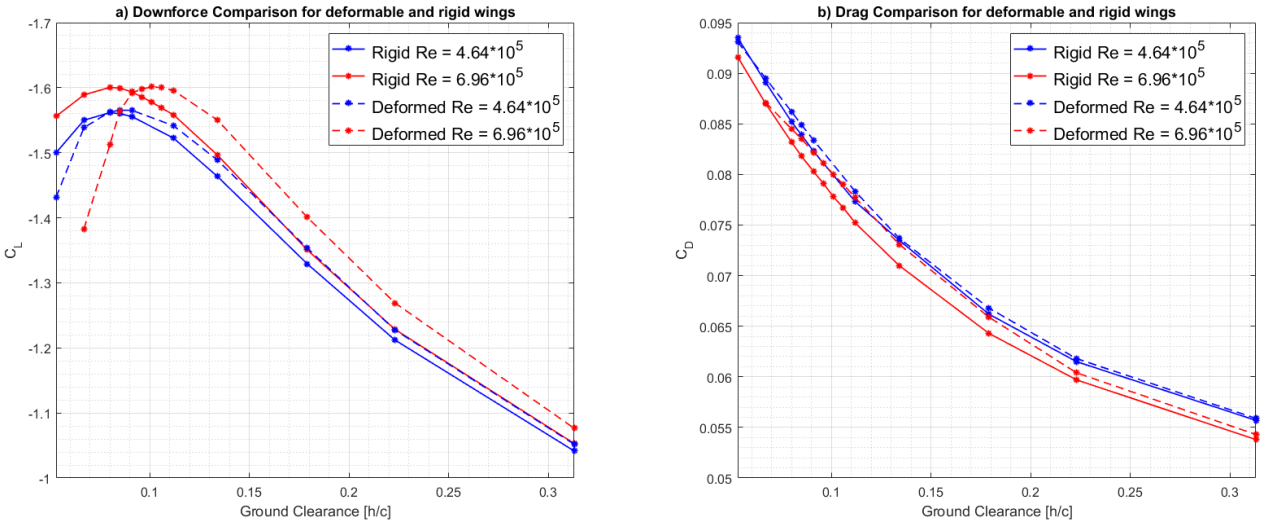

Figure 4.7: Deflection in point C and Wing twist at Reynolds number of 4.64×10^5 and 6.96×10^5

Three scenarios, $h = 0.080c, 0.101c, 0.223c$ at Reynolds number of 6.96×10^5, are used to analyse the effects of wing deflection on the flow structures. The higher Reynolds number cases are chosen as the changes from a rigid wing to a flexible wing are more evident. The $h = 0.080c$ scenario is analysed since it is the critical height when the wing is rigid but lays in the downforce loss region when the wing is flexible (Figure 4.6). The $h = 0.101c$ case is investigated as it is located in the downforce increment at low rate region for a rigid wing and represents the critical height for a flexible wing. Lastly, the $h = 0.223c$ case is selected because it is found in the downforce enhancement region for both rigid and flexible wings.

It is seen in Figure 4.8 the implications of aeroelasticity on the pressure coefficients across the wingspan, which are once again collected at $1/4c$ downstream of the leading edge. In all cases, due to wing aeroelasticity, the Cp on the bottom surface of the wing experiences significant changes, while the Cp on the top surface has minimal variations. When the wing is positioned at $h = 0.101c$ and $h = 0.223c$, the wing deflection intensifies the negative pressure across the entire wingspan. On

the other hand, at $h = 0.080c$, the wing deformation produces a loss in suction. Furthermore, it is demonstrated that the Cp distribution of flexible and rigid wings, at their respective critical heights, are notably similar, justifying why both cases have same C_L values. Small differences are observed near the tip and near the symmetry plane, where the flexible wing respectively shows slightly higher and lower suction measurements.

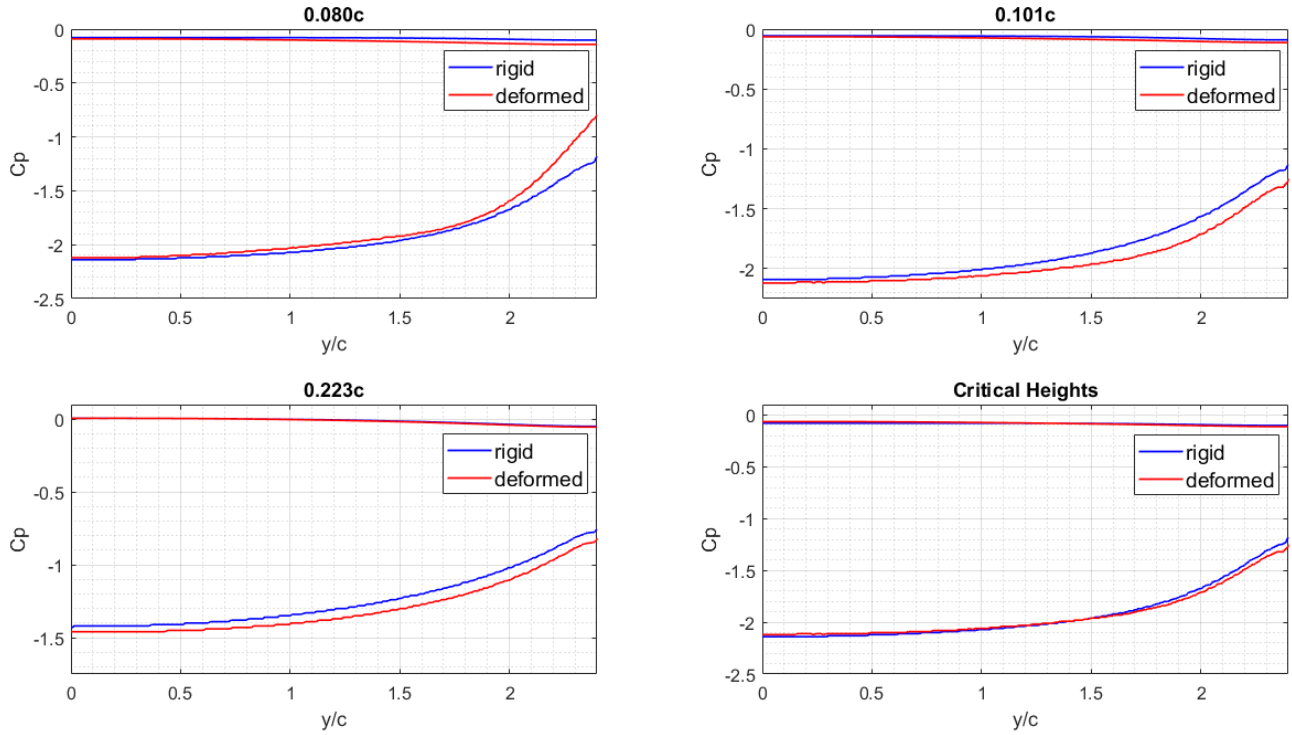

Figure 4.8: Pressure Coefficient at x = 1/4c for ground clearances of h = 0.080c, h = 0.101c and h = 0.223c

The greater suction region on the deformed wing at $h = 0.101c$ and $h = 0.223c$ is a result of the larger flow acceleration underneath the wing. The deformation enhances the venturi effect by decreasing the area underneath the wing and hence leading the flow to higher velocities. This conclusion explains why the increase in suction at $h = 0.101c$ and $h = 0.223c$ is higher close to the wing tip. Near this region, the deflection is maximum, leading to the greatest reduction in area. This effect, nevertheless, does not justify why a downforce loss is observed for the flexible wing at $h = 0.080c$.

The wall shear stress plots in Figure 4.9 showcases that, for all ground clearances, the wing flexibility intensifies the flow separation as a consequence of the enhanced venturi effect. Moreover, at $h = 0.080c$, the separation and upwash regions have their shapes drastically changed due to the wing deformation, indicating an alteration in the main tip vortex. The wall shear stress of both critical

heights, i.e., the rigid wing at $h = 0.080c$ and the flexible wing at $h = 0.101c$, shows that both separation regions have a similar overall area but slightly differ in shape. The separation region on the rigid wing at $h = 0.080c$ exhibits a constant width across the wingspan until it is influenced by the main tip vortex. On the other hand, for the flexible wing at $h = 0.101c$, the separation width slightly increases from the symmetry plane to the region in which it is affected by the main tip vortex. This is again related to the flow velocity, which is slower close to the symmetry plane.

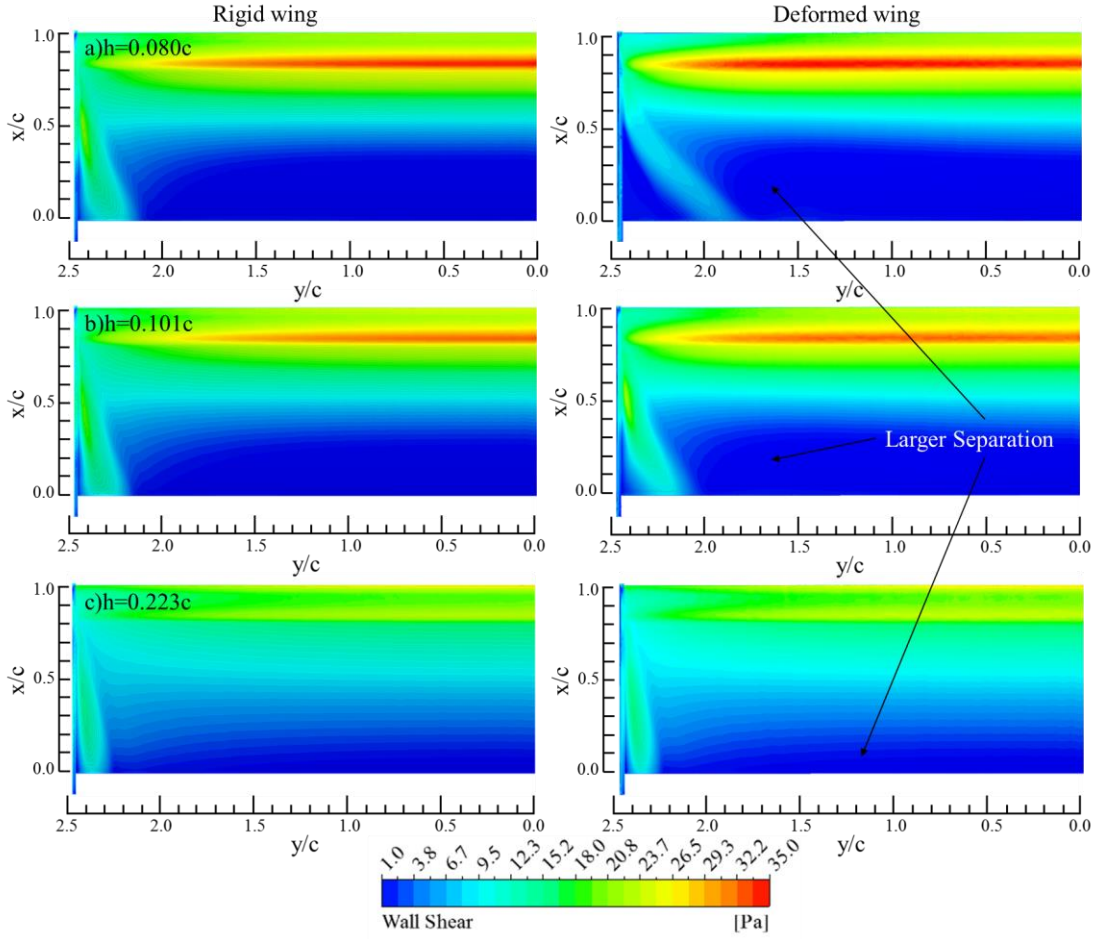

Figure 4.9: Wall-shear stress contours of a rigid (left) and of a flexible (right) wing - a) h = 0.080c; b) h = 0.101c; c) h = 0.223c. Flow direction: from top to the bottom of the page.

In order to investigate the changes in the main vortex and in the upwash effect, vorticity plots at 1.25c downstream of the leading edge are presented (Figure 4.10). They reveal that, due to the wing deformation, the main tip vortex strengthens at $h = 0.223c$ (downforce enhancement region), while it bursts at $h = 0.101c$ (critical height). At $h = 0.080c$ when the wing is deformable, there is no more main tip vortex formation. There is only the leading vortex that has its size amplified and is responsible for a small upwash effect, which is observed in the wall shear contours. These results are aligned with the conclusions achieved by Zhang et al (2002), which were commented in Section 2.3.

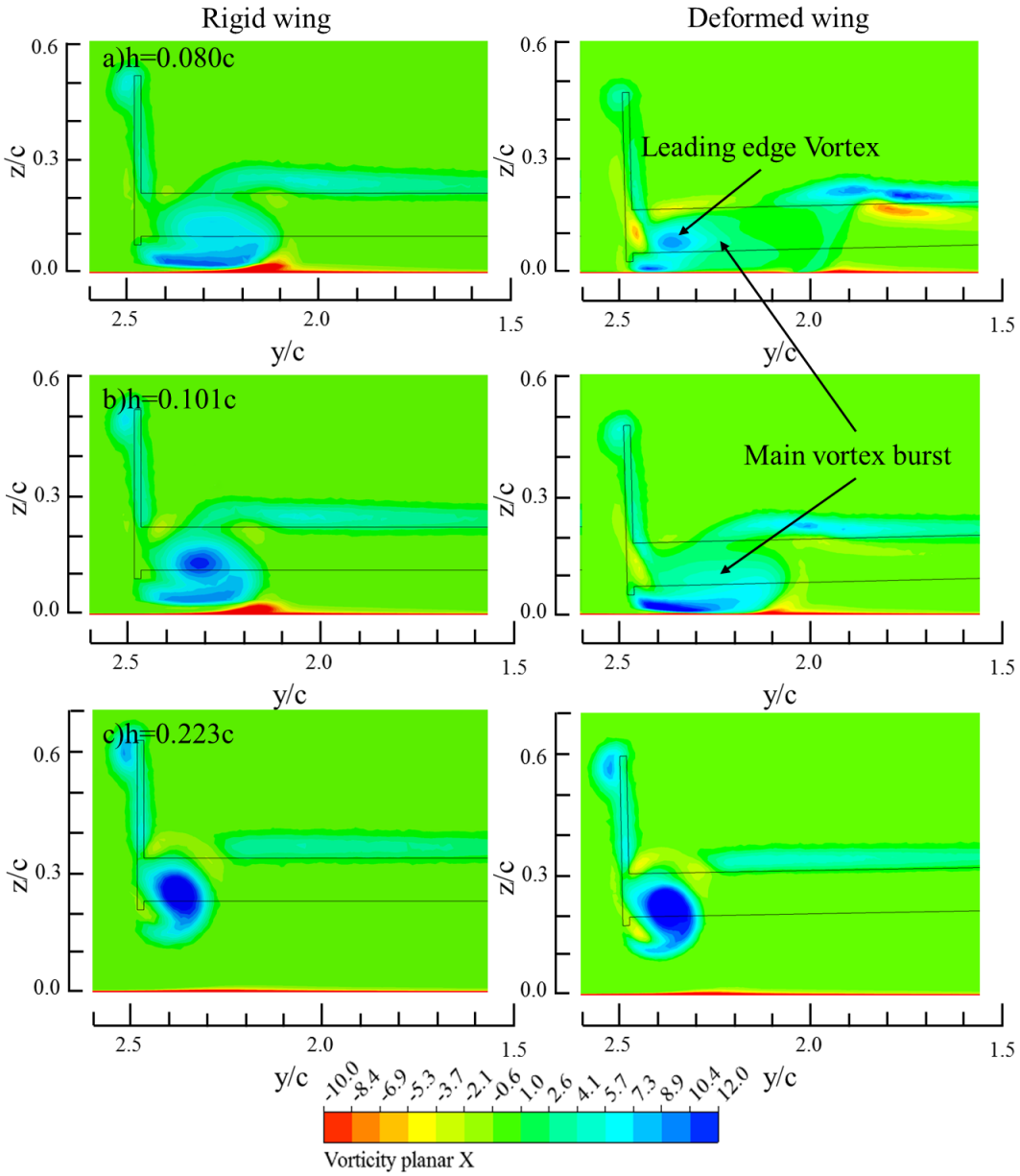

Figure 4.10: Q-criterion of a rigid (left) and of a flexible (right) wing - a) h = 0.080c; b) h = 0.101c; c) h = 0.223c. Flow direction: into the page

Figure 4.11 shows the coefficient of pressure at $y = 2.3c$. It is demonstrated that the suction peak is amplified for all deformed cases, and minimal variations in the chord-wise peak location are found. Additionally, it is seen that the flexible wing at $h = 0.080c$ presents an excessive adverse pressure gradient, which is related to the boundary layer separation and the vortex breakdown. Mudkavi (1993) stated that the vortex breaks down when the axial flow decelerates along the vortex axis, which, in the present thesis, is a result of the boundary layer separation. The comparison of both critical height plots reveals that the Cp peak of a rigid and a flexible wing have similar values, around -1.5. This indicates that a further gain in negative pressure peak prevents the flow to have a smooth

pressure recovery, generating a large adverse pressure gradient that leads to the boundary layer separation, flow deceleration and, finally, to the vortex breakdown.

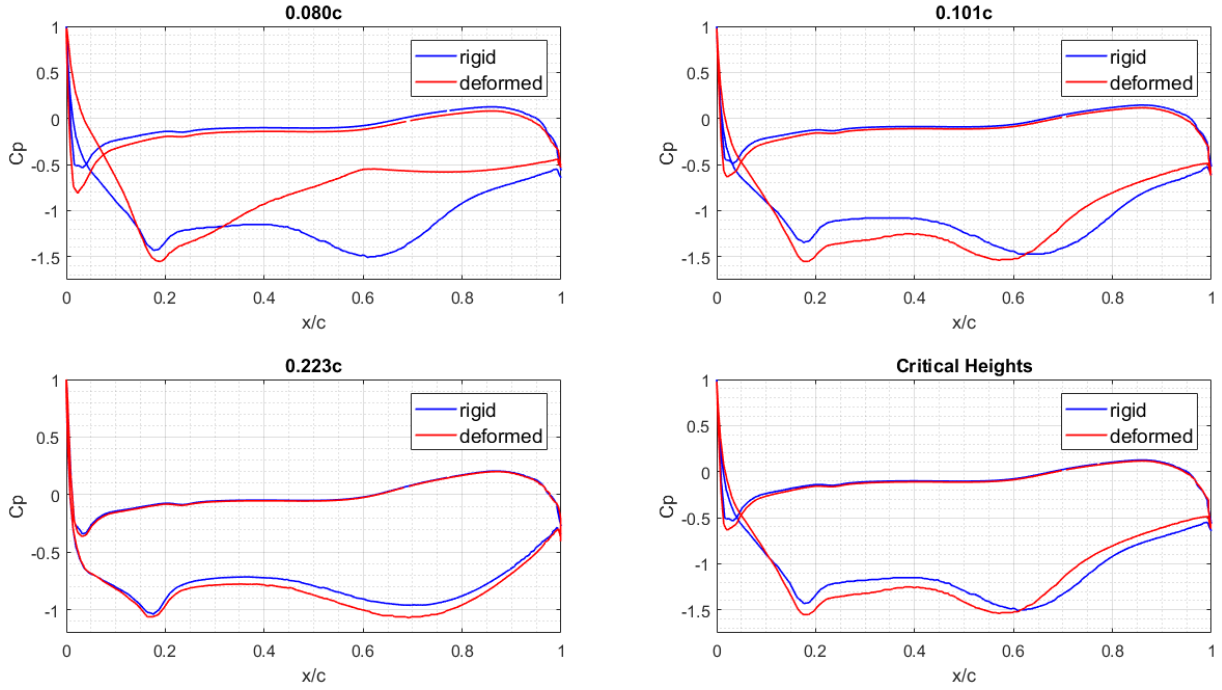

Figure 4.11: Pressure coefficient at y = 2.3c for ground clearances h = 0.080c, h = 0.101c and h = 0.223c

From the results exhibited, it is concluded that flexible and rigid wings do present different aerodynamic performance, especially at high speeds and when the wing has low bending rigidity. The wing deflection results in the enhancement of the venturi effect and/or in the earlier vortex breakdown. The enhanced venturi effect is the predominant phenomenon in the downforce increase at high rate region. In the downforce increase at low rate region, the earlier vortex breakdown starts to oppose the venturi effect. In the downforce loss region, the earlier vortex breakdown is the main effect and leads to excessive boundary layer separation.

5. Conclusion and Future Work

5.1 Conclusion

This thesis investigated the impact of aeroelasticity on a wing in ground effect. Firstly, a tightly-coupled FSI and a static loosely-coupled FSI methodologies were developed and evaluated at ground clearances of $0.112c$ and $0.134c$. Downforce, drag, wing deflection and required computational time for both FSI methodologies were compared in order to select the most efficient strategy. Then, utilising the chosen method, aeroelastic analyses were conducted at ground clearances ranging from $0.053c$ to $0.313c$ for Reynolds number of 4.64×10^5 and 6.96×10^5 in order to inspect how a rigid and flexible wing differ in ground proximity.

The results achieved by both FSI strategies presented excellent agreement, even though the static loosely-coupled method exhibited a physical inaccuracy when transferring the loads from the CFD solver to the Mechanical solver. The maximum discrepancy visualised for time-averaged measurements of downforce, drag and deflection were respectively 0.73%, 0.67% and 2.59%. Furthermore, the variations in angle of attack due to wing flexibility were minimal in both methods. However, a large difference in computational efficiency was observed between them. The tightly coupled FSI was at least 21 times more expensive than the static loosely-coupled. Indicating, therefore, that the static loosely-coupled was the most suitable method to be performed for this study.

The initial investigations of a rigid wing in ground effect showed that the increase in Reynolds number resulted in an overall gain between 1.35% and 2.6% in downforce, and a reduction in drag by 2.3% to 3.5%, which is consistent with the study of Doig et al. (2011). However, the variation in Re did not lead to any variation in the critical height when the wing was considered completely rigid. When the wing was assumed as a deformable body, the critical height shifted from $0.080c$ to $0.091c$ for the lower Re, while it varied from $0.080c$ to $0.101c$ for the higher Re. The greater aerodynamic forces measured at the higher Re explained why the aeroelastic implications are more evident. Therefore, it is expected that variations in wing's stiffness will also influence the critical height value.

Flow structure analyses showcased that, in comparison to the rigid wing, the wing deflection increased the downforce for ground clearances above the critical height by enhancing the venturi effect. The shift in critical height was attributed to the earlier vortex breakdown, which is a result of excessive boundary layer separation. The wing deflection led to an increase in negative pressure

coefficient until approximately -1.5, this higher suction peak prevented the flow to experience a smooth pressure recovery, resulting in boundary layer separation, flow deceleration and vortex breakdown.

In summary, the wing deflection can enhance the venturi effect and/or generate an earlier vortex breakdown. When the wing moves from free stream to ground proximity, the deflection increases the venturi effect until the vortex breakdown opposes it and becomes the most significant effect, resulting in a reduced downforce gain or in an increased downforce loss.

5.2 Future Work

In this study, both CFD and Structural solvers were separately verified and validated. However, the coupling system was not validated since no experimental data for flexible wings in ground effect has ever been published. Therefore, experimental analyses should be performed in order to validate the results achieved numerically.

The wing studied here is made of ABS. This material was selected taking into consideration its low Young's Modulus and possible future experimental analyses at Macquarie University, where a wing can easily be 3D printed. Nevertheless, race car and airplane wings are made of composites. Thus, it is suggested to conduct FSI analyses on wings whose torsional and bending stiffness are similar to those in reality since the mechanical properties will affect the aerodynamic performance.

With respect to the coupling methods, the first most direct development would be to solve the mapping issue associated to the static loosely-coupled FSI by developing an external code responsible for computing the pressure difference between two coupling steps, as mentioned in Section 3.3. For the tests conducted here, the mapping error did not result in large inaccuracies as the wing only deflected by small amounts, but for larger deformations, such issue will introduce large discrepancies. Furthermore, the computational efficiency of the tightly-coupled method should be improved. A significant rate of the processing time was spent in transferring information and writing files.

Tightly-coupled FSI simulations should also be performed on wings positioned close to the critical height in order to investigate whether stall flutter is likely to happen or not. If it does happen, then it should be determined the range of ground clearances in which such phenomenon could happen. Therefore, it would be possible to determine when it is necessary to employ the tightly-coupled method instead of the static loosely-coupled.

References

Abbot, I., Von Doenhoff, A.E., 1958. Theory of Wing Sections. New York: Dover.

Aftab, S.M.A., Rafie, A.S.M., Razak, N.A., Ahmad, K.A., 2016. Turbulence model selection for low reynolds number flows. PLoS ONE 11, 1–15. https://doi.org/10.1371/journal.pone.0153755

Agathangelou, B., Gascoyne, M., 1998. Aerodynamic design considerations of a Formula 1 racing car. SAE Technical Paper.

AIAA, 1998. AIAA guide for the verification and validation of computational fluid dynamics simulations. American Institute of aeronautics and astronautics.

Ashby, M.F., Cebon, D., 1993. Materials selection in mechanical design.

BBC, 2018. 2018 Austrian Grand Prix Results. URL https://www.bbc.com/sport/formula1/2018/austrian-grand-prix/results/qualifying (accessed 10.25.18).

Beer, F.P., Johnston, E.R., Dewolf, J.T., 2001. Mechanic of Materials, 3'd ed. McGraw-Hill Higher Education, Boston, MA.

Birnbaum, W., 1924. Das ebene Problem des schlagenden Flügels. ZAMM-Journal of Applied Mathematics and Mechanics/Zeitschrift für Angewandte Mathematik und Mechanik 4, 277–292.

Bleischwitz, R., De Kat, R., Ganapathisubramani, B., 2015. Aeromechanics of Membrane Wings in Ground-Effect, in: 45th AIAA Fluid Dynamics Conference. Presented at the 45th AIAA Fluid Dynamics Conference, American Institute of Aeronautics and Astronautics, Dallas, TX. https://doi.org/10.2514/6.2015-2764

Burnett, B., 2016. Coupled Fluid-Structure Interaction Modeling of a Parafoil.

Celik, I., Zhang, W.-M., 1995. Calculation of numerical uncertainty using Richardson extrapolation: application to some simple turbulent flow calculations. Journal of Fluids Engineering 117, 439–445.

Chou, P.Y., 1945. On Velocity Correlations and the Solutions of the Equations of Turbulent Fluctuation Author (s): P . Y . CHOU Source : Quarterly of Applied Mathematics , Vol . 3 , No . 1 (APRIL , 1945), pp . 38-54 Published by : Brown University Stable URL : http://www.jstor.org 3, 38–54.

Collar, A.R., 1946. The expanding domain of aeroelasticity. The Aeronautical Journal 50, 613–636.

Cross, M., Croft, T.N., Slone, A.K., Williams, A.J., Christakis, N., Patel, M.K., Bailey, C., Pericleous, K., 2007. Computational modelling of multi-physics and multi-scale processes in parallel. International Journal for Computational Methods in Engineering Science and Mechanics 8, 63–74.

Diasinos, S., 2009. The aerodynamic interaction of a rotating wheel and a downforce producing wing in ground effect. School of Mechanical and Manufacturing Engineering.

Diasinos, S., Barber, T.J., Doig, G., 2013. Influence of wing span on the aerodynamics of wings in ground effect. Proceedings of the Institution of Mechanical Engineers, Part G: Journal of Aerospace Engineering 227, 569–573. https://doi.org/10.1177/0954410011434884

Diasinos, S., Doig, G., Barber, T.J., 2014. On the interaction of a racing car front wing and exposed wheel. The Aeronautical Journal 118, 1385–1407. https://doi.org/10.1017/S0001924000010113

Doig, G., Barber, T.J., Neely, A.J., 2011. The influence of compressibility on the aerodynamics of an inverted wing in ground effect. Journal of fluids engineering 133, 061102.

Dominy, R.G., 1992. Aerodynamics of Grand Prix Cars. Proceedings of the Institution of Mechanical Engineers, Part D: Journal of Automobile Engineering 206, 267–274. https://doi.org/10.1243/PIME_PROC_1992_206_187_02

Dowell, E.H., Curtiss, H.C., Scanlan, R.H., Sisto, F., 1989. A modern course in aeroelasticity. Springer.

Du, G., Sun, M., 2010. Effects of wing deformation on aerodynamic forces in hovering hoverflies. Journal of Experimental Biology 213, 2273–2283.

Eberhardt, S., Benedict, K.A., Hedges, L., Robinson, A., Peddiraju, P., Papadopoulos, A., Skaperdas, V., Tinoco, E.N., 2014. Inclusion of Aeroelastic Twist into the CFD Analysis of the Twin-Engine NASA Common Research Model, in: 52nd Aerospace Sciences Meeting. Presented at the 52nd Aerospace Sciences Meeting, American Institute of Aeronautics and Astronautics, National Harbor, Maryland. https://doi.org/10.2514/6.2014-0251

Fairuz, Z.M., Abdullah, M.Z., Yusoff, H., Abdullah, M.K., 2013. Fluid structure interaction of unsteady aerodynamics of flapping wing at low Reynolds number. Engineering Applications of Computational Fluid Mechanics 7, 144–158.

Fluent, 2006. FLUENT 6.3 user's guide.

Garrick, I.E., Reed III, W.H., 1981. Historical Development of Aircraft Flutter. Journal of Aircraft 18, 897–912. https://doi.org/10.2514/3.57579

Habchi, C., Russeil, S., Bougeard, D., Harion, J.-L., Lemenand, T., Ghanem, A., Valle, D.D., Peerhossaini, H., 2013. Partitioned solver for strongly coupled fluid–structure interaction. Computers & Fluids 71, 306–319. https://doi.org/10.1016/j.compfluid.2012.11.004

Heinrich, R., Ahrem, R., Gunther, G., Kersken, H.-P., Kruger, W., Neumann, J., 2001. Aeroelastic computation using the AMANDA simulation environment. DGLR BERICHT 19–30.

Heyder-Bruckner, J., Zhang, X., 2010. Detached-Eddy Simulation of a Double-Element Wing in Ground Effect, in: 48th AIAA Aerospace Sciences Meeting Including the New Horizons

Forum and Aerospace Exposition. Presented at the 48th AIAA Aerospace Sciences Meeting Including the New Horizons Forum and Aerospace Exposition, American Institute of Aeronautics and Astronautics, Orlando, Florida. https://doi.org/10.2514/6.2010-59

Jung, S.N., Sa, J.H., You, Y.H., Park, J.S., Park, S.H., 2013. Loose fluid-structure coupled approach for a rotor in descent incorporating fuselage effects. Journal of Aircraft 50, 1016–1026.

Katz, J., 1995. Race car aerodynamics. Robert Bentley.

Keogh, J., Doig, G., Diasinos, S., Barber, T., 2015. The influence of cornering on the vortical wake structures of an inverted wing. Proceedings of the Institution of Mechanical Engineers, Part D: Journal of Automobile Engineering 229, 1817–1829.

Kesti, J., Olsson, S., 2014. Fluid structure interaction analysis on the aerodynamic performance of underbody panels 54.

Keye, S., Rudnik, R., 2015. Validation of Wing Deformation Simulations for the NASA CRM Model using Fluid-Structure Interaction Computations, in: 53rd AIAA Aerospace Sciences Meeting. Presented at the 53rd AIAA Aerospace Sciences Meeting, American Institute of Aeronautics and Astronautics, Kissimmee, Florida. https://doi.org/10.2514/6.2015-0619

Keyes, D.E., McInnes, L.C., Woodward, C., Gropp, W., Myra, E., Pernice, M., Bell, J., Brown, J., Clo, A., Connors, J., 2013. Multiphysics simulations: Challenges and opportunities. The International Journal of High Performance Computing Applications 27, 4–83.

Knowles, K., Donoghue, D., 1994. A study of wings in ground effect. Presented at the Loughborough University Conference on Vehicle Aerodynamics, pp. 1–13.

Kolmogorov, A.N., 1941. Dissipation of energy in locally isotropic turbulence, in: Dokl. Akad. Nauk SSSR. pp. 16–18.

Landajuela, M., Vidrascu, M., Chapelle, D., Fernández, M.A., 2017. Coupling schemes for the FSI forward prediction challenge: comparative study and validation. International journal for numerical methods in biomedical engineering 33, e2813.

Launder, B.E., Sharma, B.I., 1974. Application of the energy-dissipation model of turbulence to the calculation of flow near a spinning disc. Letters in Heat and Mass Transfer 1, 131–137. https://doi.org/10.1016/0094-4548(74)90150-7

Launder, B.E., Spalding, D.B., 1972. Lectures in mathematical models of turbulence. Academic Press, London; New York.

Lin, S., Han, X., Bi, Y., Ju, S., Gu, L., 2017. Fluid-Structure Interaction in Abdominal Aortic Aneurysm: Effect of Modeling Techniques. BioMed Research International 2017, 1–10. https://doi.org/10.1155/2017/7023078

Love, M., De La Garza, T., Charlton, E., Egle, D., 2000. Computational aeroelasticity in high performance aircraft flight loads. ICAS Paper 1.

Mahon, S., Zhang, X., 2006. Computational Analysis of a Inverted Double-Element Airfoil in Ground Effect. Journal of Fluids Engineering 128, 1172. https://doi.org/10.1115/1.2353268

Malalasekera, W., Versteeg, H.K., 2006. An Introduction to Computational Fluid Dynamics - The Finite Volume Method, AIAA Journal. https://doi.org/10.2514/1.22547

McBeath, S., 1998. Competition car downforce: a practical guide. GT Foulis.

Menter, F.R., 1994. Two-equation eddy-viscosity turbulence models for engineering applications. AIAA journal 32, 1598–1605.

Molina, J., Zhang, X., 2011. Aerodynamics of a Heaving Airfoil in Ground Effect. AIAA Journal 49, 1168–1179. https://doi.org/10.2514/1.J050369

Molina, J., Zhang, X., Angland, D., 2011. On the unsteady motion and stability of a heaving airfoil in ground effect. Acta Mechanica Sinica 27, 164–178. https://doi.org/10.1007/s10409-011-0445-9

Mudkavi, V.Y., 1993. The phenomenon of vortex breakdown.

Piquee, J., Breitsamter, C., 2017. Numerical and Experimental Investigations of an Elasto-Flexible Membrane Wing at a Reynolds Number of 280,000. Aerospace 4, 39. https://doi.org/10.3390/aerospace4030039

Potsdam, M., Yeo, H., Johnson, W., 2006. Rotor airloads prediction using loose aerodynamic/structural coupling. Journal of Aircraft 43, 732–742.

Ranzenbach, R., Barlow, J., 1997. Multi-element airfoil in ground effect-An experimental and computational study, in: 15th Applied Aerodynamics Conference. p. 2238.

Ranzenbach, R., Barlow, J., 1996. Cambered airfoil in ground effect-an experimental and computational study. SAE Technical Paper.

Ranzenbach, R., Barlow, J., 1995. Cambered airfoil in ground effect-wind tunnel and road conditions, in: 13th Applied Aerodynamics Conference. p. 1909.

Ranzenbach, R., Barlow, J.B., 1994. Two-dimensional airfoil in ground effect, an experimental and computational study. SAE Technical Paper.

Roberts, L.S., Correia, J., Finnis, M.V., Knowles, K., 2016. Aerodynamic characteristics of a wing-and-flap configuration in ground effect and yaw. Proceedings of the Institution of Mechanical Engineers, Part D: Journal of Automobile Engineering 230, 841–854.

Rodriguez, A., 2007. Morphing aircraft technology survey, in: 45th AIAA Aerospace Sciences Meeting and Exhibit. p. 1258.

Rojratsirikul, P., Wang, Z., Gursul, I., 2010. Effect of pre-strain and excess length on unsteady fluid–structure interactions of membrane airfoils. Journal of Fluids and Structures 26, 359–376.

Schäfer, M., 2006. Computational engineering: introduction to numerical methods. Springer.

Shih, T.-H., Liou, W.W., Shabbir, A., Yang, Z., Zhu, J., 1995. A New k-ε Eddy Viscosity Model for High Reynolds Number Turbulent Flows. Compurers Fluids 24, 227–238. https://doi.org/10.1016/0045-7930(94)00032-T

Shirk, M.H., Hertz, T.J., Weisshaar, T.A., 1986. Aeroelastic tailoring-theory, practice, and promise. Journal of Aircraft 23, 6–18.

Shyy, W., Klevebring, F., Nilsson, M., Sloan, J., Carroll, B., Fuentes, C., 1999. Rigid and flexible low Reynolds number airfoils. Journal of Aircraft 36, 523–529.

Spalart, P., Allmaras, S., 1992. A one-equation turbulence model for aerodynamic flows, in: 30th Aerospace Sciences Meeting and Exhibit. Presented at the 30th Aerospace Sciences Meeting and Exhibit, American Institute of Aeronautics and Astronautics, Reno,NV,U.S.A. https://doi.org/10.2514/6.1992-439

Sylt, C., 2018. Revealed: The $2.6 Billion Budget That Fuels F1's 10 Teams [WWW Document]. URL https://www.forbes.com/sites/csylt/2018/04/08/revealed-the-2-6-billion-budget-that-fuels-f1s-ten-teams/#4563da736595 (accessed 10.25.18).

Theodorsen, T., 1949. General theory of aerodynamic instability and the mechanism of flutter.

Thuwis, G.A.A., De Breuker, R., Abdalla, M.M., Gürdal, Z., 2010. Aeroelastic tailoring using lamination parameters: Drag reduction of a Formula One rear wing. Structural and Multidisciplinary Optimization 41, 637–646. https://doi.org/10.1007/s00158-009-0437-6

Uekermann, B.W., 2016. Partitioned fluid-structure interaction on massively parallel systems. Technische Universität München.

Vann Doormal, J., Raithby, G.D., 1984. Enhancement of the SIMPLE method for predictingg incompressible flows. Numer. Heat Transfer 7, 147–163.

Versteeg, H.K., Malalasekera, W., 2007. An introduction to computational fluid dynamics: the finite volume method. Pearson Education.

Von Baumhauer, A.G., Koning, C., 1923. On the stability of oscillations of an airplane wing.

Vrchota, P., Prachař, A., Šmíd, M., 2017. Improvement of Computational Results of NASA Airliner Model by Wing Modal Analysis. Journal of Aircraft 54, 1294–1302. https://doi.org/10.2514/1.C033952

Wang, Y., Lin, Y., 2008. Combination of CFD and CSD packages for fluid-structure interaction. Journal of Hydrodynamics 20, 756–761.

Weisshaar, T.A., 1995. Aircraft aeroelastic design and analysis. School of Astronautics and Aeronautics-Purdue University, Class Notes.

Wilcox, D., 1993. Turbulence Model for CFD.

Yasue, K., Ueno, M., 2016. Model Deformation Corrections of NASA Common Research Model Using Computational Fluid Dynamics. Journal of Aircraft 53, 951–961. https://doi.org/10.2514/1.C033445

Zerihan, J., 2001. An investigation into the aerodynamics of wings in ground effect. University of Southampton.

Zerihan, J., Zhang, X., 2000. Aerodynamics of a single element wing in ground effect. Journal of aircraft 37, 1058–1064.

Zhang, X., Zerihan, J., Ruhrmann, A., Deviese, M., 2002. Tip vortices generated by a wing in ground effect, in: Proceedings of the 11th International Symposium on Applications of Laser Techniques to Fluid Mechanics. Citeseer.

Zienkiewicz, O.C., Taylor, Robert Leroy, Zienkiewicz, O.C., Taylor, Robert Lee, 1977. The finite element method. McGraw-hill London.

Appendix

Appendix A: Geometry Dimensions and Boundary Conditions

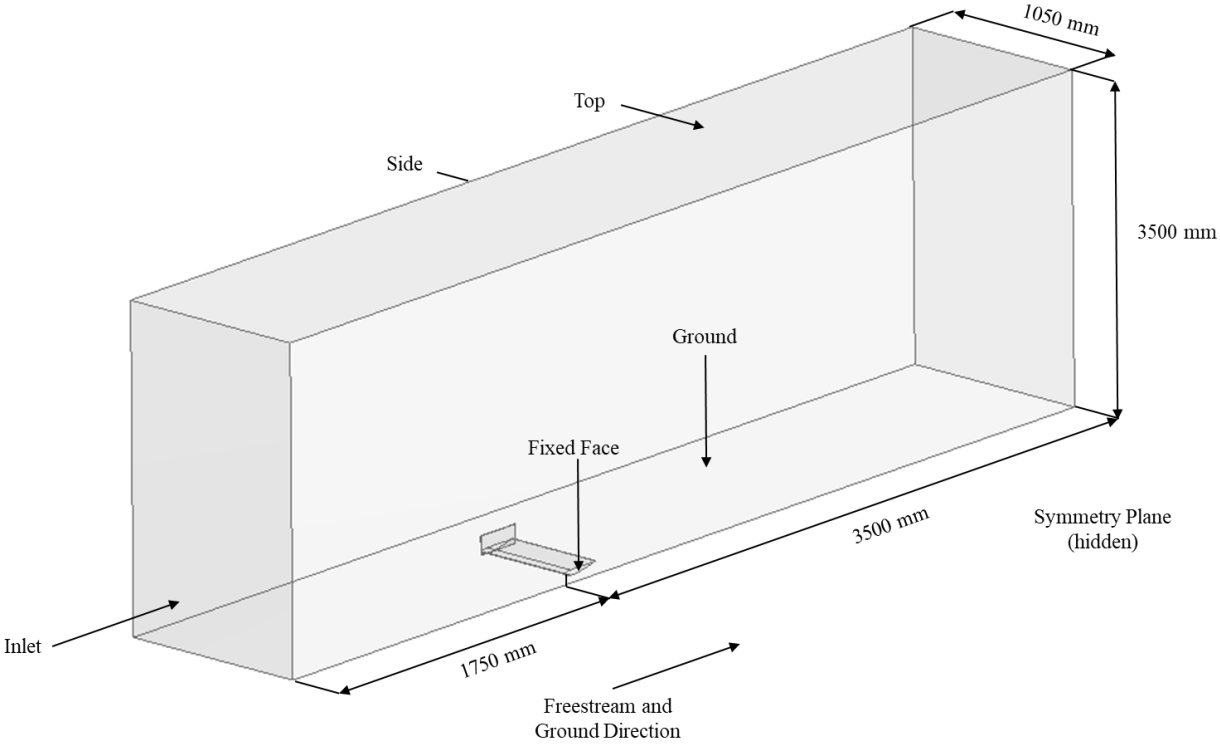

Figure A.0.1: Fluid domain and boundaries of the computational model[‡]

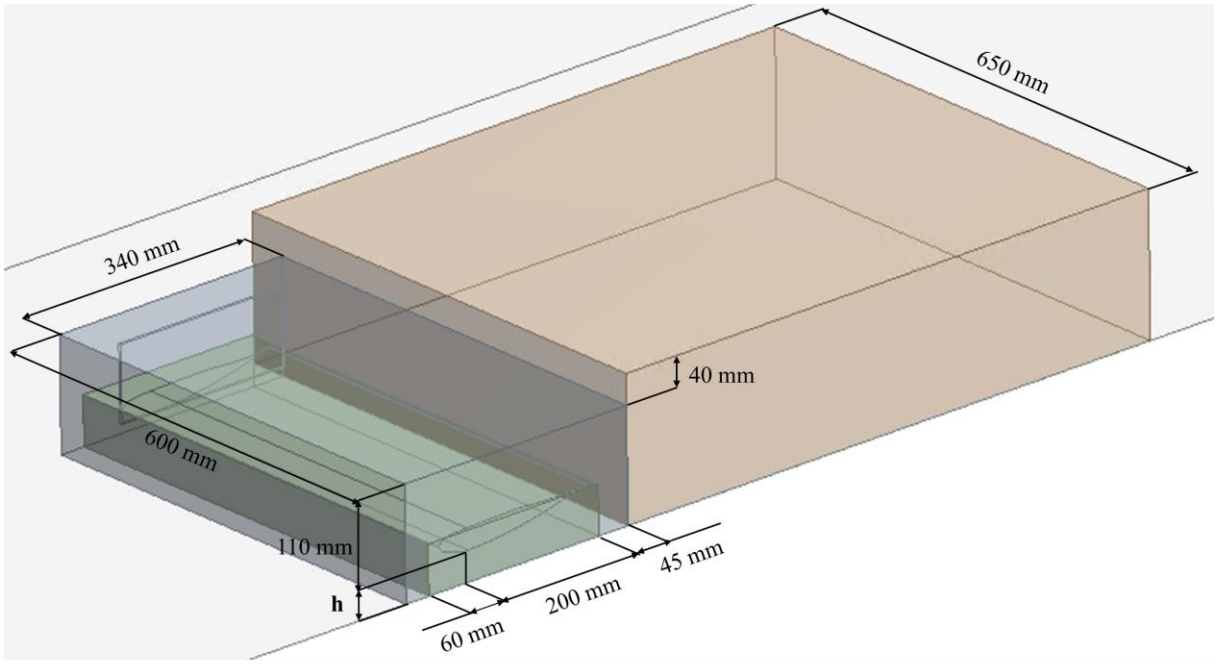

Figure A.0.2: Body of influence dimensions

[‡] Bodies of influence hidden

Appendix B: Wing model

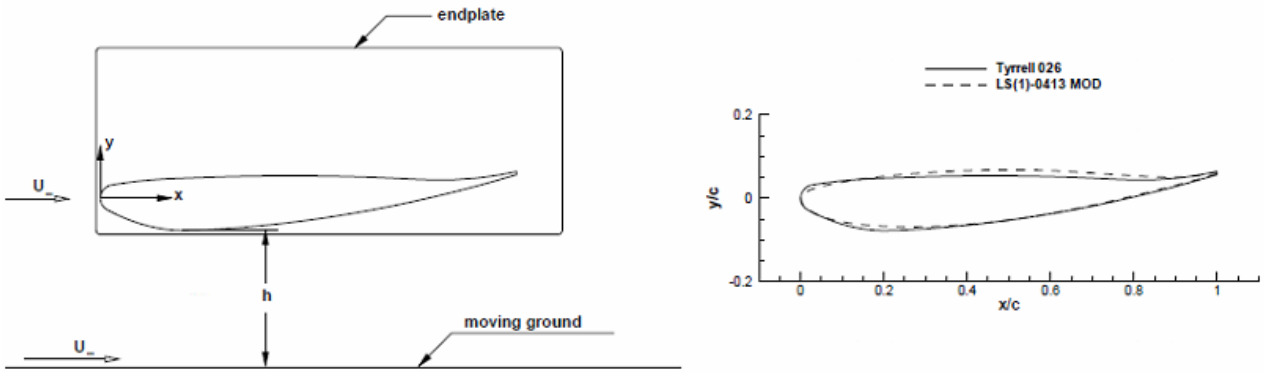

Figure B.0.1: Wing model3

Appendix C: CFD Mesh

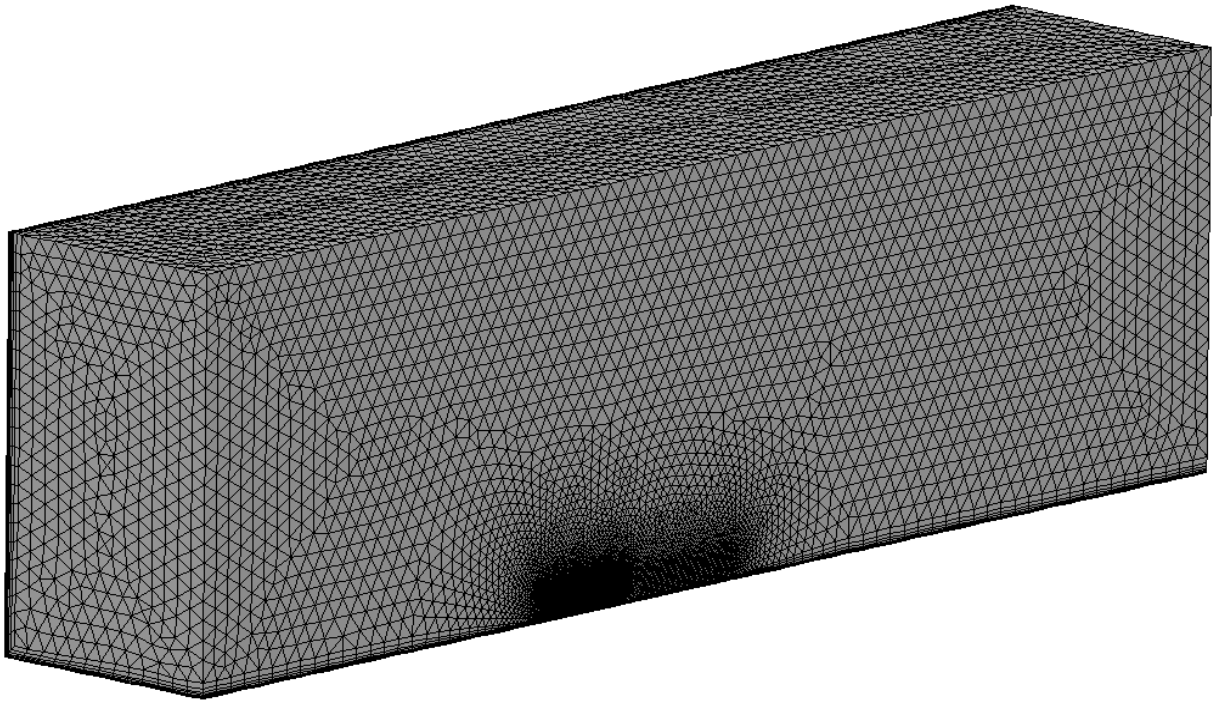

Figure C.0.1: CFD Mesh

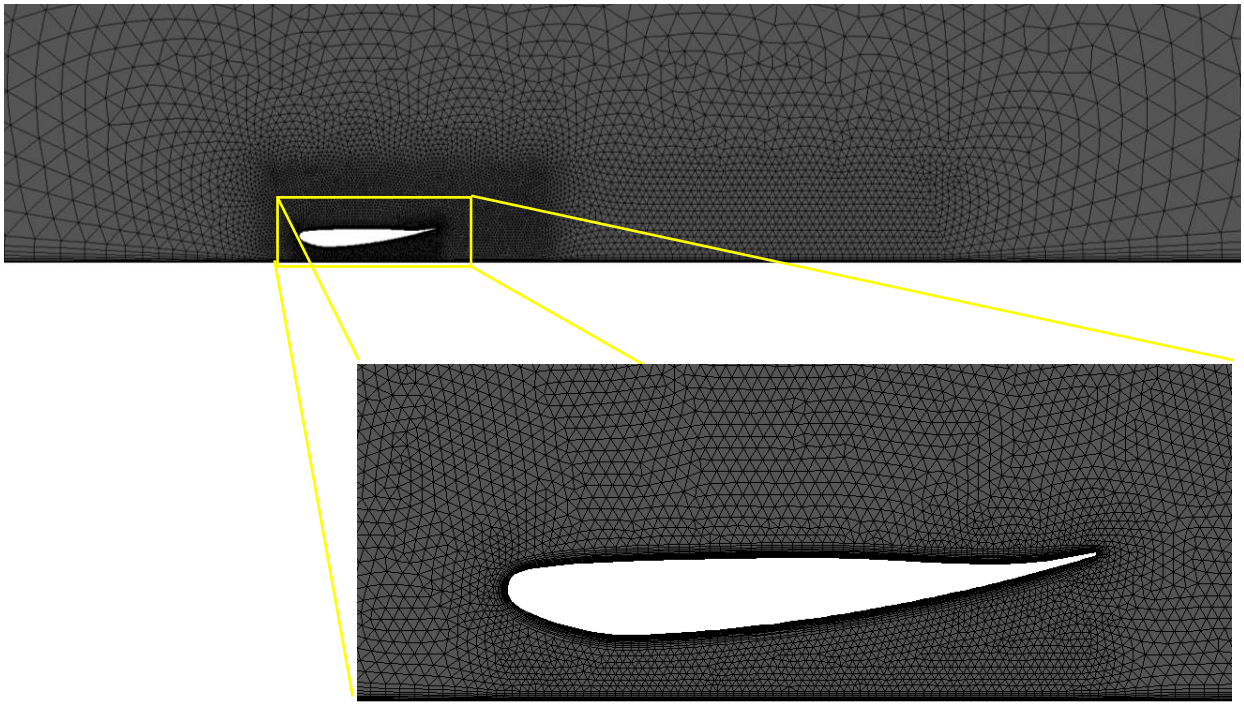

Figure C.0.2: CFD Mesh around wing

Appendix D: Mechanical Mesh

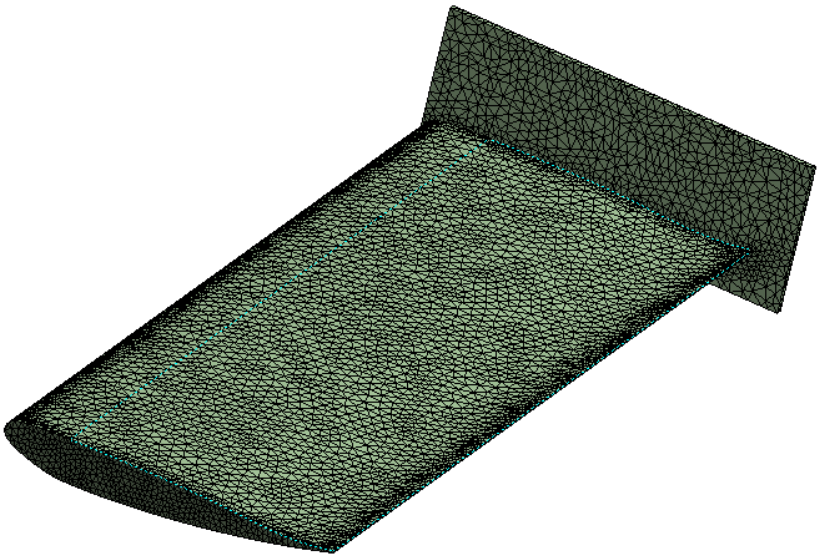

Figure D.0.1: Mechanical Mesh

Appendix E: GCI Formulation

$$E_1 = \frac{\varepsilon}{r^p - 1}$$

$$E_2 = \frac{r^p \varepsilon}{r^p - 1}$$

$$\varepsilon = \frac{f_2 - f_1}{f_2}$$

$$r = \frac{H_2}{H_1}$$

$$GCI = F_s |E_1|$$

$$F_s = 3$$

$$p = 3$$

f is the parameter analysed.

H is the number of cells in the mesh.

1 and 2 represent the coarse and the fine mesh respectively.

p represents the order of convergence.

F_s is the factor of safety.

Appendix F: Mechanical Solver (FEM) Validation

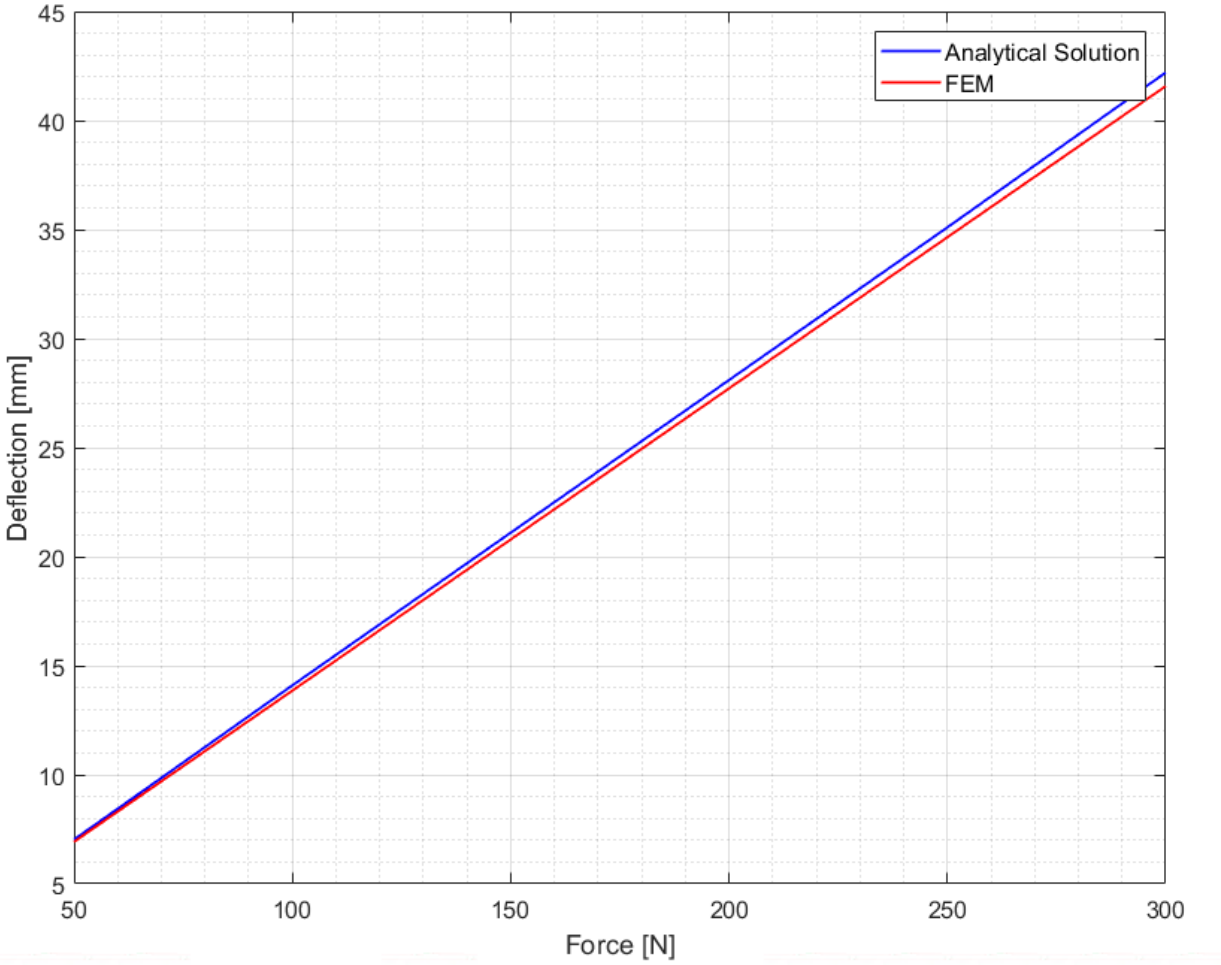

Figure F.0.1: Structural Solver Validation

Analytical solution angular coefficient:

$$m_{an} = \frac{l^3}{3E_s I} = 0.14068$$

FEM solution angular coefficient:

$$m_{FEA} = \frac{\vartheta_{P_2} - \vartheta_{P_1}}{F_2 - F_1} = \frac{41.58 - 6.93}{250} = 0.1386$$

Error:

$$\frac{m_{an} - m_{FEA}}{m_{an}} = 1.48\%$$

Appendix G: FFT Plot

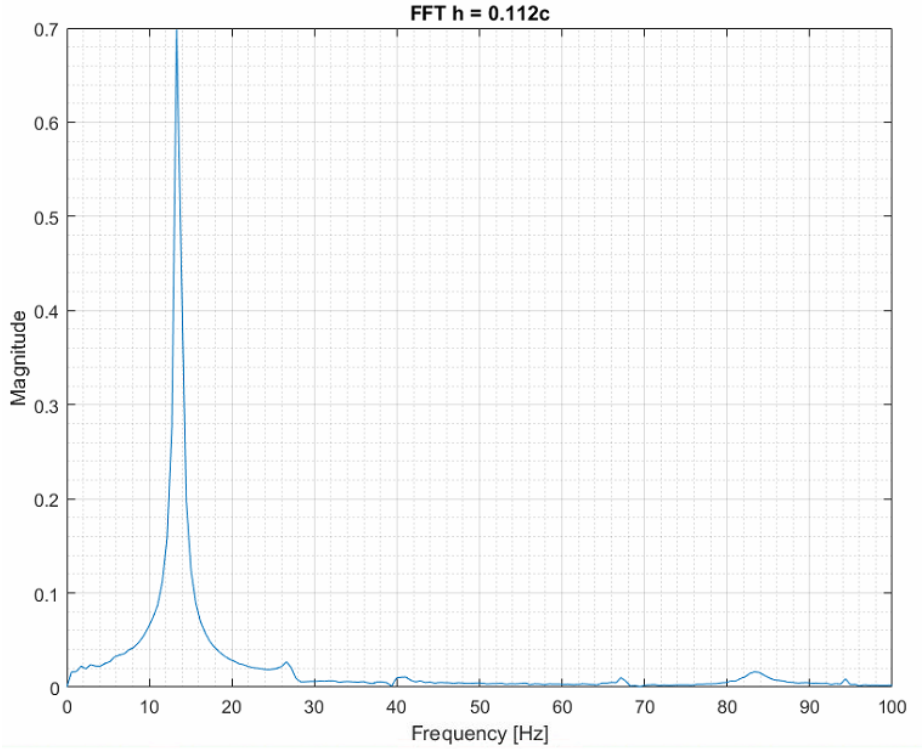

Figure G.0.1: FFT wing at h = 0.112c

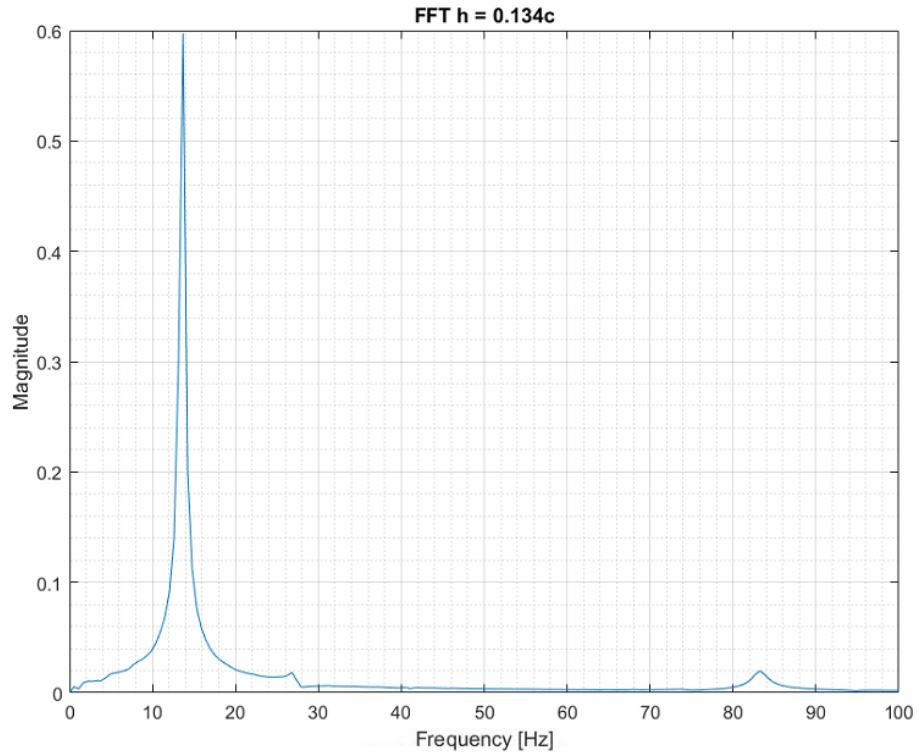

Figure G.0.12: FFT wing at h = 0.134c

Appendix H: Mapping Error

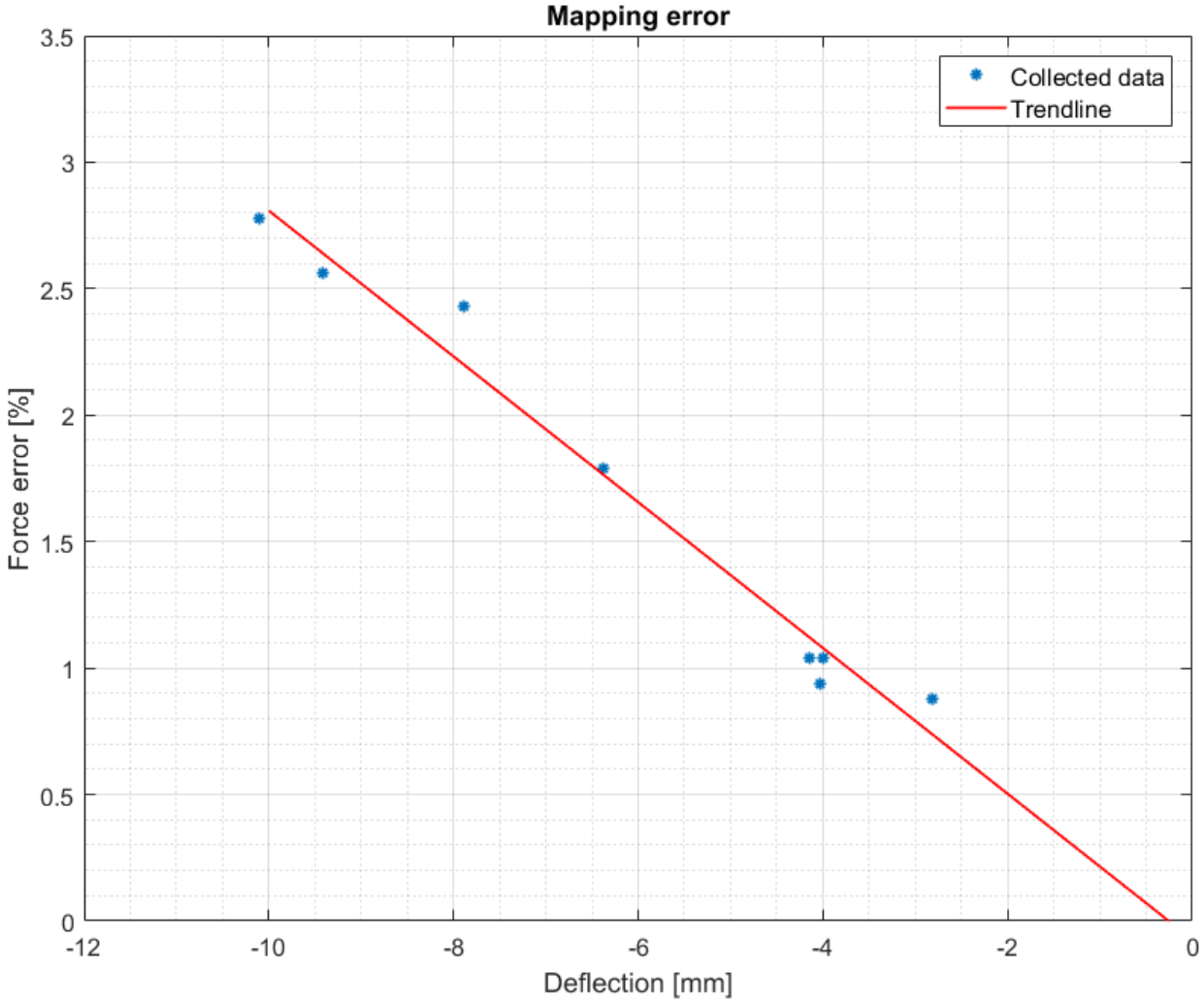

Figure H.0.1: Mapping error in function of wing deflection

Appendix I: Wall Shear-stress Comparison

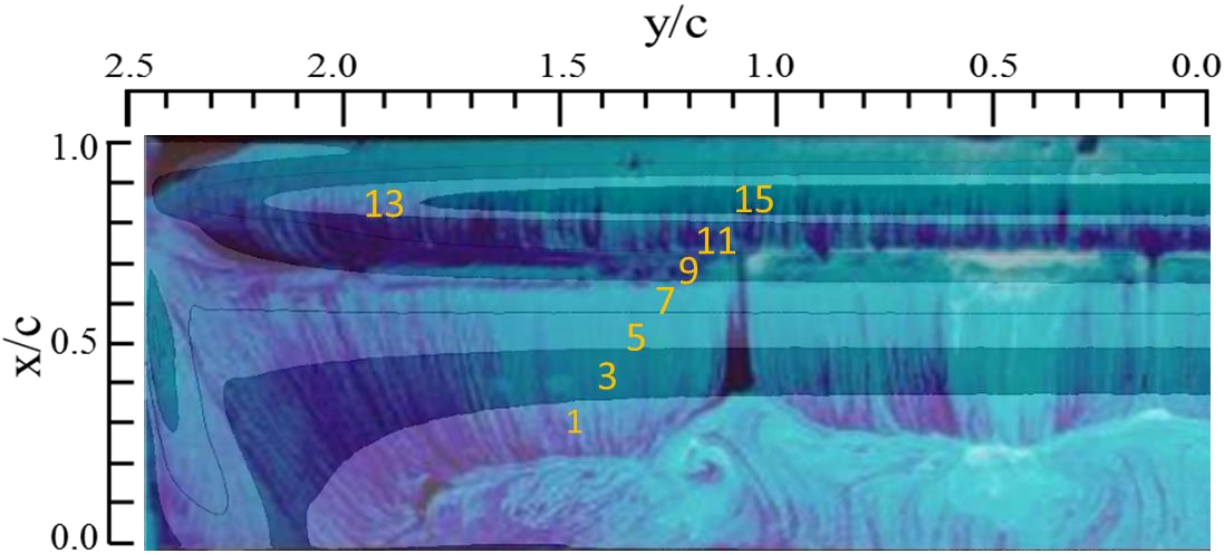

Figure I.0.1: Comparison of Zerihan's on surface flow visualisation to shear stress values numerically computed. Flow direction: from top to bottom of the page

Appendix J: Q-Criterion comparison of both FSI methods

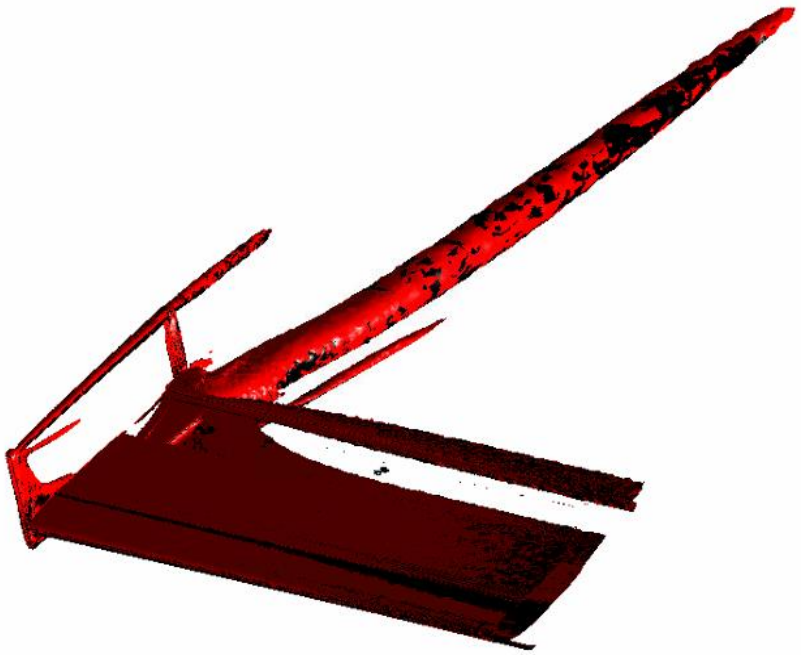

Figure J.0.1: Q-Criterion of Static-loosely coupled, in red, and Tightly-coupled (1.670), in black.

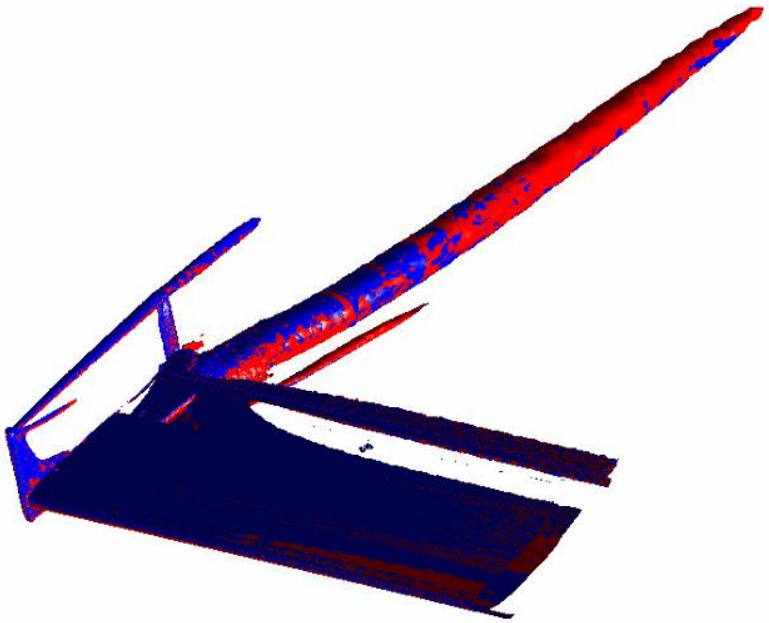

Figure J.0.2: Q-Criterion of Static loosely-coupled, in red, and Tightly-coupled (1.707s), in black

Appendix K: ABS Mechanical Properties

Property	Maximum	Minimum	Average[§]
Density (g/cm^3)	1.05	1.08	1.65
Tensile Strength (MPa)	33.1	51.7	42.4
Yield Strength (MPa)	29.6	48.3	38.95
Young's Modulus (GPa)	1.97	2.48	2.25
Poisson's ratio	0.393	0.409	0.401

Table K.0.1: ABS Mechanical properties (Ashby and Cebon, 1993)

[§] The average values of the material properties were used in the simulations